

## Diagenetic analysis of shallow and deep-seated gas hydrate systems from the Bay of Bengal

Virsen Gaikwad<sup>1,2</sup>, Firoz Badesab<sup>1\*</sup>, Mahender Kotha<sup>2</sup>

<sup>1</sup> CSIR - National Institute of Oceanography, Dona Paula, 403004, Goa, India.

<sup>2</sup> School of Earth Ocean and Atmospheric Sciences, Goa University, 403206, Goa, India.  
Corresponding author: Dr. Firoz Badesab (firoz@nio.org)

### Abstract

This is the first systematic high-resolution rock magnetic study complemented by mineralogical and petrological observations conducted on sediment cores representing shallow (active cold seep; SSD-45/Stn-4/GC-01) and deep-seated (NGHP-01-15A) gas hydrate systems in the Bay of Bengal which addresses two key questions: (i) how magnetic minerals respond to the geochemical environment at two different diagenetic settings experiencing variable fluid sequence, and (ii) elucidates the control on the magnetite and greigite authigenesis in sulfidic, methanic, and gas hydrate bearing sediments. Titanomagnetite is the dominant detrital magnetic mineral identified in the studied cores from the Krishna-Godavari (K-G) basin along with diagenetic (pyrite) and authigenic (magnetite, greigite) minerals. Large detrital titanomagnetite and silicate-hosted (fine-grained) magnetic inclusions survived diagenetic dissolution during high sedimentation events. Magnetic proxies (ARM/SIRM and SIRM/ $\chi_{lf}$ ) provided useful insights on the diagenetic and authigenic formation and preservation of magnetic particles in the studied cores. Preferential diagenetic dissolution of finer (detrital) magnetic particles in sulfidic and authigenic formation of magnetite in methanic environment is clearly evident in the ARM/SIRM record of cores from both sites. Elevated values of SIRM/ $\chi_{lf}$  in cores SSD-45/Stn-4/GC-01 (sulfidic and hydrate bearing) and NGHP-01-15A (methanic) indicate formation and preservation of ferrimagnetic authigenic (SP) greigite particles. Based on the magnetic proxies, we demonstrated that the formation of authigenic magnetite in the methanic environment of both sites is tightly linked with the microbial iron-reduction process. Multiple occurrences of authigenic carbonate provided evidence on the episodic intensification of anaerobic oxidation of methane (AOM) at active seep and silicate weathering coupled to microbial methanogenesis at deep-seated gas hydrate site respectively.

**Keywords:** Diagenesis, Magnetic Minerals, Active Cold Seep, Gas Hydrates, Authigenic Magnetite, Greigite, Bay of Bengal.

### Key Highlights:

- Unravels the diagenesis and authigenesis of magnetic minerals in shallow and deep-seated gas hydrate systems from the Bay of Bengal.
- Magnetite and greigite authigenesis is tightly linked with microbial iron reduction process.
- Magnetic inclusion within host silicates shielded the magnetic particles from sulfidic pore fluids and survived diagenetic dissolution.
- A schematic model explains the controls on the evolution of magnetic mineralogies in two diagenetic systems experiencing variable fluid sequences.

## 1. Introduction

Marine sediments across large parts of the Krishna-Godavari (K-G) basin offshore, India contain abundant methane and gas hydrates. The K-G basin represents an ideal natural laboratory with its unique presence of shallow (active cold seep; SSD-45/Stn-4/GC-01; Mazumdar et al., 2019) and deep-seated (NGHP-01-15A; Collett et al., 2008; Kumar et al., 2014) gas hydrate systems to obtain a comprehensive view of the methane-related diagenetic and authigenic processes in the two different marine gas hydrate systems. Magnetic minerals at active, paleo, and relict methane seep sites and in sediments influenced by past anaerobic oxidation of methane (AOM) processes are the potential archive of past fluid sequences and provide an important constraint on the methane-related diagenetic and authigenic processes (Dewangan et al., 2013; Musgrave et al., 2019; Greve et al., 2021; Gaikwad et al., 2021; Kars et al., 2021). Geochemical processes linked with fluid migration, gas hydrate formation/dissociation favour the growth of iron sulphides which induce a magnetic signature in the host sediments (Esteban et al., 2008). For example, sulfate-reduction driven by AOM generates hydrogen sulfide in the pore water via bacterial activities (Canfield and Berner 1987). The linkage between rock magnetism, pore-water geochemistry, methane-related magnetic mineral diagenesis, and authigenesis has been well-explored (Roberts, 2015). Authigenic formation of ferrimagnetic (greigite, magnetite) and non-magnetic (pyrite) iron sulfides in methanic sediments are influenced by the history of fluid sequence and gas hydrate dynamics (formation/dissociation) (Dewangan et al., 2013; Kars and Kodama, 2015; Roberts, 2015). Previous rock magnetic studies dealing with magnetic mineral diagenesis in methanic and gas hydrate bearing sediments has established the linkage between methane-related geochemical and microbial processes and sediment magnetism. For example, in Mackenzie Delta, Canada (Enkin et al., 2007), Mediterranean continental shelf (Amiel et al., 2020), North-western Weddell Sea (Reilly et al., 2020), South China Sea (Lin et al., 2021), Hikurangi Margin, New Zealand (Greve et al., 2021; Kars et al., 2021), Izu-Bonin rear arc (Musgrave et al., 2019), Nankai Trough (Kars and Kodama, 2015; Shi et al., 2017) and offshore Shimokita Peninsula (Phillips et al., 2017) Japan, Bay of Bengal (Dewangan et al., 2013; Badesab et al., 2019; Gaikwad et al., 2021; Johnson et al., 2021), offshore Taiwan (Horng, 2018), Cascadia Margin (Musgrave et al., 2006; Larrasoana et al., 2007), Arctic Vestnesa Ridge, offshore western Svalbard (Johnson et al., 2014), West Siberian Sea (Rudmin et al., 2018), and offshore Taiwan (Horng, 2018).

Detrital magnetic particles undergo a reduction process manifested by progressive diagenetic dissolution and subsequent transformation into intermediate ferrimagnetic iron sulfide (greigite) or stable non-magnetic (pyrite) minerals (Roberts, 2015). Magnetic methods bear the potential to rapidly characterize the detrital, diagenetic, authigenic magnetic minerals in terms of their concentration, grain

size, and mineralogy (Esteban et al., 2008). Previous rock-magnetic studies dealing with magnetic mineral diagenesis in the K-G basin mainly focussed on elucidating the controls of structural and diagenetic (early vs. late) processes on the sediment magnetism in an active and relict seep sites (Gaikwad et al., 2021), unravelling the linkage between greigite magnetism, methane seepage dynamics, and evolution of active cold seep site associated with shallow gas hydrate system (Badesab et al., 2020a), developing a novel magnetic based approach for the exploration of gas hydrates (Badesab et al., 2019), magnetic mineral diagenesis in a paleo-cold seep site (Dewangan et al., 2013), constraining the formation and preservation of greigite in methanic sediments (Badesab et al., 2020b; Gaikwad et al., 2021), isolating detrital and diagenetic signals in methane-bearing marine sediments (Johnson et al., 2021), influence of high-energy depositional environment on the magnetic mineral diagenesis and formation of gas hydrates (Badesab et al., 2020b). However, a focused rock magnetic study directly dealing with the diagenetic analysis of two different (shallow *versus* deep-seated) marine gas hydrate systems in the K-G basin is still lacking.

Sediment cores retrieved during Council of Scientific and Industrial Research (CSIR)-National Institute of Oceanography (NIO) gas hydrate discovery cruise (SSD-045 onboard R/V Sindhu Sadhana) and first Indian National Gas Hydrate Drilling Expedition (NGHP-Exp-01) provided an excellent opportunity to illuminate the multiple methane-influenced geochemical processes that impact sediment magnetization of the continental margin hydrate system (Collett et al., 2008; Kumar et al., 2014). In this study, we conducted comprehensive rock magnetic investigations complemented by mineralogical and petrological observations on the sediment cores representing shallow (active cold seep) and deep-seated gas hydrate systems to examine (1) how magnetic minerals respond to the geochemical environment at two different diagenetic (shallow versus deep gas hydrate system) settings experiencing variable fluid sequence, and (2) elucidate the control on the magnetic mineral authigenesis in methanic sediments.

## **2. Geological Setting**

The K-G basin is a proven petroliferous basin situated in the central-eastern continental margin of India (ECMI) (Fig. 1a). The basinal area is about 28,000 km<sup>2</sup> onshore and 145,000 km<sup>2</sup> offshore (Rao, 2001). A sediment thickness is about 3–5 km in the onshore and 8 km in the offshore region (Prabhakar and Zutshi, 1993; Bastia, 2007). The sediments in the basin are fed by two major river systems (Krishna and Godavari) and their tributaries. Both the rivers drain through the Late Cretaceous Deccan Basalts (DcB), Archean-Proterozoic Gneissic Complexes (APGC), and recent sediments (Ramesh and Subramanian 1988; Sangode et al., 2007) and deliver a large amount of detrital (magnetite-rich) sediments to the K-G basin (Ramesh and Subramanian 1988; Sangode et al., 2007). Geological and

geophysical studies have established the presence of active and paleo-cold seep associated with shallow and deep-seated gas hydrates in the K-G basin (Collett et al., 2008; Mazumdar et al., 2009; Mazumdar et al., 2019; Dewangan et al., 2021; Gaikwad et al., 2021). Several geomorphic structures such as mounds, shale diapirs, and faults are formed as a result of ongoing neo-tectonics in the K-G basin. Methane migration through the fault/fractures supported the formation of gas hydrate deposits in the K-G basin (Dewangan et al., 2010; Shankar and Riedel, 2010).

Continental margins worldwide store immense quantities of methane gas (Kvenvolden, 1993). Cold seeps (active, relict, paleo) and gas hydrates (shallow and deep-seated gas hydrates) are characteristics of many active continental margins (Suess, 2014). Discovery of active cold seep associated with shallow (fracture-filled; Mazumdar et al., 2019; Dewangan et al., 2021) and deep-seated (massive and disseminated-type; Collett et al., 2008; Collet et al. 2014; Kumar et al. 2014; Collett et al., 2019) gas hydrates in the K-G basin, Bay of Bengal during a dedicated gas hydrate exploration cruises onboard R/V Sindhu Sadhana (SSD-45, 2018) and D/V JOIDES Resolution (NGHP Expedition-01, 2006) has placed India on a global gas hydrate distribution map. At shallow (active cold seep) hydrate site, gas chimneys and shale-tectonism driven by faults/fractures are the two main fluid migration pathways (Dewangan et al., 2010, 2021; Sriram et al., 2020). The occurrence of shallow gas hydrates (2-3 mbsf) and active methane seepage at this site is predominantly controlled by the migration of fluids along deep-rooted faults and the presence of deeper gas reservoir in the K-G basin (Mazumdar et al., 2019; Dewangan et al., 2021). Methane-rich fluid flow at this site is inferred by the presence of chemosynthetic biological communities and authigenic carbonates on the seafloor (Mazumdar et al., 2019; Gaikwad et al., 2021). Gas hydrate at site NGHP-01-15 mainly occurs as pore-filling disseminated-type predominantly in sand-rich intervals (~75 to 81 mbsf) mostly as channel-levee deposits (Riedel et al., 2011; Collett et al., 2014). Deep sourced fluid and gas migration produced hydrate saturation up to 68% in a coarse-grained stratigraphic horizon at this site (Solomon et al., 2014). The moussey texture formed due to gas hydrate dissociation was observed in the clean sand and this was further confirmed through pore water chloride (~28 mbsf, 60 mbsf, 79 mbsf, and 87 mbsf) and temperature (~79 mbsf) anomalies (Collet et al., 2008). The present-day sulfate-methane transition zone (SMTZ) depth at this site is at 31.5 mbsf (Fig. S7; Collet et al., 2008). The sulfate concentration profile of the uppermost 30 mbsf showed S-shaped pattern probably due to the influence of recent high sedimentation events (Fig. S7; Collet et al., 2008; Solomon et al., 2014). The entire recovered sedimentary sequence of core NGHP-01-15A was defined as one lithostratigraphy unit based on the physical and sedimentological properties. Sediment lithology comprised of nanofossil-bearing to -rich clay, and silty clay that ranges in color from dark brown, dark grey, greenish black to black in the

uppermost intervals (Collet et al., 2008). Sand/silt laminae and beds are abundant and occur in discrete zones throughout the core. About 5–8 m thick sediment interval characterized by the highest sand content was found in this core (Riedel et al., 2014). High porosity and permeability offered by these coarse-grained sand layers favored gas hydrate formation and accumulation at this site (Collett et al., 2008, 2014). Shell fragments, foraminifera, and authigenic carbonates (nodule, band, cement) occur throughout the core. The carbonate mineralogy is comprised of iron and calcium-rich carbonate and low and high magnesium calcite (Teichert et al., 2014). Clay mineralogy at this site is dominated by the higher content of smectite (36% to 76%) with appreciable amount of illite (10% to 29%), kaolinite (9% to 31%), and chlorite (3% to 11%) in the bulk sediment sample (Phillips et al., 2014). The total organic carbon (TOC) in core NGHP-01-15A ranges between 0.86 to 3.18%, except at 87 mbsf where TOC content is much higher (10.17 %). The calcium carbonate ( $\text{CaCO}_3$ ) content ranges from 0.38 to 29.62 % (Johnson et al., 2014).

## **2. Methods**

Room, low-and high-temperature magnetic measurements, FORC analysis, and SEM observations provide diagnostic features that can be used to identify and characterize the magnetic mineral assemblages in the studied sediment cores (Liu et al., 2012).

### **2.1. Sediment core lithology, sampling, and measurements**

A short (2.23 m) gravity core (SSD-45/Stn-4/GC-01) was retrieved from active cold seep site (SSD-45/Stn-4 (Lat: 15°43.0411'N, Lon: 82°04.0599'E, water depth = 1803 m, recovered core length: 2.23 m) associated with shallow gas hydrates during a dedicated gas hydrate exploration cruise (SSD-45) of CSIR-NIO onboard R/V Sindhu Sadhana. The sediment core was sub-sampled at every 2 cm interval. After opening the core onboard, light gray to deep black colored sediments yielded strong smell of hydrogen sulfide. Multiple yellowish-brown colored authigenic carbonate layers were noticed in the uppermost (0 to 1.57 mbsf; Fig. 8a-g; Table. 1) sediment interval. Live chemosynthetic communities were observed on the seafloor at this site (Fig. 8h-k). Fracture-filled type gas hydrates were recovered from three (1.77 - 1.85 mbsf, 2.07 - 2.11mbsf, and 2.17 - 2.23 mbsf) sediment intervals in this core (Fig. 8l). To prevent the exposure of samples to atmospheric conditions, the sub-sampling of sediment core was carried out in the presence of high purity nitrogen flushing. A 196.45 m long drilled sediment core NGHP-01-15A (Lat: 16°05.6983'N, Lon: 082° 09.7467'E, water depth = 926 m, recovered core length: 200.0 m) was retrieved during the first Indian NGHP, Exp-01(Collett et al., 2014, Riedel et al., 2014) onboard D/V JOIDES Resolution from high-energy sediment depositional site (NGHP-01-15) in the K-G basin (Fig. 1; Collett et al., 2008). The entire sediment core (NGHP-

01-15A) was sub-sampled at intervals of 1.5–6 m on each 9.6 m long sections onboard. The sub-samples were further transported and stored at ~ 5-6°C cold storage repository of CSIR-NIO, Goa, India. The bulk sediment sub-samples were dried, weighed, and packed in the 25 mm plastic sample bottles. Mass-dependent magnetic susceptibility was measured on these packed samples. The comparison between shipboard multi-sensor core logger (MSCL) derived magnetic susceptibility (in 2006; Collet et al., 2008) and laboratory-based mass-specific magnetic susceptibility (in December 2020; present study) showed the minimum alteration of the magnetic signals after core collection and storage (Fig. S5). Magnetic measurements were carried out in the Paleomagnetic Laboratory of CSIR-NIO India. The specialized rock magnetic measurements on selective samples were carried out at the Centre for Advanced Marine Core Research (CMCR), Kochi University, Japan.

## 2.2. Magnetic measurements

Low-field low frequency (0.47 kHz) magnetic susceptibility ( $\chi$ ) was measured on a MS2B Bartington Instruments magnetic susceptibility meter. All remanent magnetizations were measured using an AGICO JR-6A spinner magnetometer. An anhysteretic remanent magnetization (ARM) was imparted using a 100 mT alternating magnetic field superimposed on a fixed direct current (DC) bias field of 50  $\mu$ T. An isothermal remanent magnetization (IRM) was applied in an inducing field of +2T in the forward direction and was demagnetized by DC backfields at -20, -30, -100, and -300 mT using a MMPM10 pulse magnetizer. Mass-normalized IRM acquired at a peak field of 2T is assumed as the saturation IRM (SIRM). S-ratio is calculated as the ratio between the IRM at -300 mT and SIRM ( $IRM_{-300mT}/SIRM_{2T}$ ; Bloemendal et al., 1992).

Thermomagnetic analyses were conducted on a Natsuhara Giken (Model NMB-89) magnetic balance (Range: Room temperature to 700°C) with a heating rate of 10°C/min in a 0.3-T field at the Paleo and Rock Magnetism Laboratory of CMCR. Magnetic hysteresis loops, first-order reversal curves (FORC), and back-field demagnetization curves were measured for nine selected dried sediment samples with a saturating field of 1T, field increment of 4 mT, slew rate limit of 1 T/s, and averaging time of 200 ms at the CMCR. Processing of FORC diagrams were done using the FORCinel software (smoothing factor (SF) = 5; Harrison and Feinberg, 2008).

Low-temperature magnetic measurements were made on five selected dried sediment samples with a Quantum Design Magnetic Properties Measurement System at CMCR. An RT-SIRM was applied at room temperature (300 K) in a 2.5 T. Samples were further cooled to 5 K and warmed back again to 300 K in a zero magnetic field. A LT-SIRM was then imparted at 5 K in 2.5 T. Samples were further warmed up to 300 K in a zero magnetic field (“ZFC” for zero field-cooled). Samples were then cooled

to 5 K in the presence of a 2.5 T magnetic field. A LT-SIRM was again induced at 5 K, and samples were warmed to 300 K in a zero magnetic field (“FC” for field-cooled).

### **2.3. Mineralogical analysis**

Magnetic particles were extracted from the bulk sediment samples using a magnetic mineral extraction method developed by Petersen et al. (1986). A scanning electron microscope (SEM; JEOL JSM-5800 LV) at CSIR-NIO was used to capture the image of the magnetic particles in a secondary electron imaging mode at the energy levels between 15 and 20 keV. To determine the composition of magnetic particles, an energy dispersive X-ray spectroscopy (EDS) probe attached to the microscope was used. Sediment magnetic mineralogy was determined using a Rigaku X-Ray Diffractometer (Ultima IV). The samples were allowed to run from 15° to 65° of 2 $\theta$  at 1°/min scan speed using Cu K $\alpha$  radiation ( $\lambda = 1.5414 \text{ \AA}$ ). Optical microscopy on separated >63  $\mu\text{m}$  fractions from different sediment intervals in both cores was carried out using Olympus microscope (BX41).

### **2.4. Petrography of authigenic carbonates**

Methane-derived authigenic carbonate (MDAC) nodules at the active seep site (core SSD-45/Stn-4/GC-01) were picked up from the split sediment cores during sub-sampling. The polished thin sections (26 x 46 mm) of MDAC were prepared and further examined using petrographic microscope Trinocular Microscope (*Model No.-BX51TRF*) in the Petrology Laboratory of CSIR-NIO, Goa, India.

## **4. Results**

### **4.1. Rock magnetic record of sediment cores from shallow and deep-seated gas hydrate system**

Rock magnetic profile of sediment cores from active methane seep site associated with shallow (SSD-45/Stn-4/GC-01) and deep-seated gas hydrate (NGHP-01-15A) systems are presented in Fig. 2. A magnetically enhanced and laterally extensive band (Fig. S1) is clearly evident in the sediment magnetic record of seven long drilled cores from the K-G basin (Badesab et al., 2019). Such band represents several events of rapid sediment deposition that eventually led to the quick burial and formation of a distinct magnetite-rich sediment interval in the NGHP drilled sediment cores (Fig. S1; Shanmugam et al., 2009; Shankar and Riedel, 2010; Dewangan et al., 2011; Ramprasad et al., 2011; Krishna et al., 2016; Badesab et al., 2019; Badesab et al., 2022). Based on the down-core magnetic susceptibility ( $\chi_{\text{lf}}$ ) trends, we have demarcated the entire magnetic profile of core SSD-45/Stn-4/GC-01 from active seep (AS) site into two distinct sediment magnetic zones (Z-I, Z-II, Fig. 2). The uppermost zone of core SSD-45/Stn-4/GC-01 (Z-I: 0.01 to 1.6 mbsf) showed a general downcore decline in  $\chi_{\text{lf}}$ , ARM, and SIRM indicating reduction in the magnetic mineral concentration (Fig. 2a-c). A magnetic (SIRM/ $\chi_{\text{lf}}$ ; Snowball and Thompson, 1990; Maher and Thompson, 1999; Peters and

Dekkers, 2003) proxy for iron sulfides showed a systematic downcore decrease suggesting the loss of fine and subsequent increase in coarse-grained magnetic particles except few intervals in Z-I and Z-II (Fig. 2e). Anomalous drop in S-ratio (0.61 – 0.96) from 0.31 to 1.09 mbsf suggest the presence of ferrimagnetic iron sulfides (greigite, hexagonal pyrrhotite) (Fig. 2f; Peters and Dekkers, 2003; Roberts et al., 2011; Kars and Kodama, 2015; Horng, 2018). The bottom most zone (Z-II: 1.61 to 2.23 mbsf) showed marked decrease in  $\chi_{lf}$ , ARM, SIRM values suggesting drop in magnetite concentration (Fig. 2a-c). Three peaks of increase in SIRM/ $\chi_{lf}$  and  $\chi_{lf}$  in the gas hydrate bearing sediment intervals in Z-II suggest the presence of SP size ferrimagnetic iron sulfides (greigite, hexagonal pyrrhotite) (Fig. 2a,e; Snowball, 1991; Tarduno, 1995; Larrasoña et al., 2007; Rowan et al. 2009). S-ratio profile showed two trends in Z-II (Fig. 2f). The beginning of Z-II is marked by higher values of S-ratio suggesting the dominance of ferrimagnetic iron oxides. The lower most interval (1.83 to 2.23 mbsf) showed significant drop indicating the presence of high coercivity minerals or ferrimagnetic iron sulfides.

Rock magnetic profile of a deep-seated gas hydrate core (NGHP-01-15A) can be classified into five distinct sediment magnetic zones (Z-I, Z-II, Z-III, Z-IV and Z-V). A systematic downcore reduction in  $\chi_{lf}$ , ARM and SIRM in Z-I (0.74 to 17.76 mbsf) indicates decline in concentration of magnetic particles (Fig. 2g-i). The lower part (14.02 to 25.86 mbsf) of Z-I is marked by higher values of ARM/SIRM suggesting the dominance of fine-grained detrital magnetic particles in this zone (Fig. 2j; Peters and Dekkers, 2003; Liu et al., 2012). A distinct minima in  $\chi_{lf}$ , ARM and SIRM and drop in S-ratio close SMTZ (Fig. 2, Fig. S7) indicate the presence of paramagnetic (pyrite) and high coercivity minerals is Z-II (30.86 to 41.91 mbsf) (Fig. 2g-i, l). The Z-III (42.57 to 72.57 mbsf) is characterized by higher  $\chi_{lf}$ , ARM, SIRM and SIRM/ $\chi_{lf}$  values reflecting the presence of fine-grained ferrimagnetic iron sulfides of diagenetic or authigenic origin (Fig. 2g-i,k; Rowan et al., 2009; Roberts et al., 2018). A magnetic enhancement manifested by increase in  $\chi_{lf}$ , ARM, SIRM, S-ratio and relatively low ARM/SIRM indicates the presence of coarse-grained magnetic particles in Z-IV (112.85 to 140.35 mbsf) close to the present BSR depth (Fig. 2g-j,l). The Z-V (149.9 to 196.45 mbsf) is marked by a downcore rise in  $\chi_{lf}$ , ARM, SIRM and high S-ratio suggesting the period of increase in the supply of magnetic minerals (Fig. 2g-i, l). A minor downcore rise in ARM/SIRM from end of Z-II to Z-V suggest gradual increase in the proportion of fine-grained authigenic magnetic particles (Fig. 2j; Dillon and Bleil, 2006). Similarly, a trend of noticeable increase in SIRM/ $\chi_{lf}$  from Z-III i.e., below the gas hydrate occurrence zone till the bottom of the core (NGHP-01-15A) can be attributed to the increase in the growth of fine-grained ferrimagnetic iron sulfide (greigite) particles (Fig. 2k; Snowball, 1991; Larrasoña et al., 2007; Rowan et al., 2009).



## 4.2. Temperature dependant magnetic Susceptibility

The thermomagnetic curves ( $\chi$ - $T$ ) of all six analyzed samples from a shallow gas hydrate core (SSD-45/Stn-4/GC-01) showed very similar pattern (Fig. 3a). A noticeable drop in  $\chi$  values between 522°C and 632°C in majority of the samples suggest that the bulk magnetic mineralogy is dominated by magnetite and titanomagnetite (Dunlop et al., 1997). A minor rise in  $\chi$  between 352°C to 452°C for most of the samples could be attributed to the presence of titanomagnetite exhibiting wide range of Ti-contents (Lattard et al., 2006) or due to transformation of paramagnetic minerals into magnetite during heating process (Fig. 3a; Hirt and Gehring, 1991; Hirt et al., 1993; Passier et al., 2001; Philips, 2018).

In a deep-seated gas hydrate core (NGHP-01-15A),  $\chi$ - $T$  curves (Fig. 3b) show a gentle decline in magnetization from room temperature up to  $\sim 340.5$  °C (average) and increases further suddenly to values close to the initial magnetization value. The noticeable increase at  $\sim 373.51$  °C (average) is consistent with high-temperature oxidation of non-magnetic iron phases into magnetic phases (Passier et al., 2001). Increase in magnetization maintains a broad peak between  $\sim 403.5$  °C and 520.8 °C (average) that ends with a sharp drop between  $\sim 572.0$  °C and 635.3 °C (average) indicating that the bulk magnetic mineralogy in core NGHP-01-15A is dominated by magnetite and titanomagnetite (Fig. 3b; Dunlop et al., 1997).

## 4.3. Low-temperature magnetometry

Results of low-temperature magnetic measurements of selective samples from core SSD-45/Stn-4/GC-01 displays similar magnetic signatures and lacks a Verwey transition (Fig. 4; Verwey, 1939). The curves reflect the dominance of paramagnetic signal which hindered the minor changes in the magnetization. The first derivative magnetization curves are shown in Fig. 4b,d,f. A minor peak in the derivative curve near Verwey transition temperature was observed only in sample from Z-II (1.80 mbsf), which is indicative for the presence of stoichiometric magnetite in low concentration (Fig. 4d). Rapid decrease in LT-SIRM from 5 to 30 K and nearly 55 – 60 % loss of the applied remanence is noticed (Fig. 4a,c,e). This indicates the presence of superparamagnetic (SP) magnetic (rapidly unblocked) particles in these samples (Tarduno, 1995; Passier and Dekkers, 2002). We did not observe any Besnus transition typical indicator for pyrrhotite (Besnus and Meyer, 1964; Dekkers, 1989; Larrasoana et al., 2007) in the analyzed samples.

## 4.4. FORC diagrams

FORC diagrams provided important constraints on the domain states and type of magnetic minerals (Fig. 5; Roberts et al., 2000). Closed contours in all plots indicate that the magnetic particles in the analyzed samples displays vortex state to multidomain (MD) type behavior (Fig. 5a-i; Roberts et al.,

2000; Roberts et al., 2017; Roberts et al., 2018; Lascu et al., 2018). FORC's distribution in Fig. 5a-i also provide clues on the magnetic mineralogy which appears to be dominated by the ferrimagnetic iron oxides (vortex state-MD type magnetite) and sulfides (SP greigite) (Muxworthy and Dunlop, 2002).

#### **4.5. Identification of magnetic mineralogy using SEM-EDS and XRD analyses**

SEM-EDS data of magnetic particles representing different sediment intervals of core SSD-45/Stn-04/GC-01 confirmed that titanomagnetite is the major magnetic mineral in the studied cores (Fig. 6a-f, Fig. S6a-f). Several ferrimagnetic iron oxides (detrital) and sulfides (diagenetic) of different sizes are noticed in both sediment magnetic zones (Z-I, Z-II). Well-preserved as well diagenetically influenced detrital titanomagnetite grains were found to be present throughout the core (Fig. 6a-f, Fig. S6a-f). EDS data for these grains indicate the presence of titanium, iron, and oxygen with minor amount of silicon, aluminium, calcium, manganese, chromium, and magnesium. Numerous diagenetically formed iron sulfides (pyrite) occur as framboid (Fig. 6b, Fig. S6b) as well as tiny individual (Fig. 6d-e, Fig. S6d-e) grains are observed. Authigenically formed greigite particles are observed in association with larger titanomagnetite grains in Z-II (Fig. 6f, Fig. S6f). In sediment core (NGHP-01-15A) from deep-seated gas hydrates, fine as well as coarse-grained detrital titanomagnetites are found to occur throughout all sediment magnetic zones (Z-I to Z-V) (Fig. 6g-m, Fig. S6g-m). Iron sulfides were found to occur as tiny particles growing on a larger titanomagnetite grains in a magnetically reduced zone (Z-II) proximal to present-day SMTZ (Fig. 6h, Fig. S6h). High sedimentation rate interval (Z-IV) is marked by abundant coarse-grained detrital titanomagnetites (Fig. 6k-l Fig. S6k-l).

XRD analyses on magnetic particles from all sediment magnetic zones in cores SSD-45/Stn-04/GC-01 and NGHP-01-15A confirm that magnetic mineralogy is governed by titanomagnetite, greigite, and pyrite grains occurring in varying proportion (Fig. 7a-l). Dominant peaks of quartz are also noticed in all samples (Fig. 7a-l). In core SSD-45/Stn-04/GC-01, titanomagnetite, greigite, and pyrite grains are found to occur together (Fig. 7a-f). Samples from Z-II exhibiting high  $\chi_{lf}$  and SIRM/ $\chi_{lf}$  in cores SSD-45/Stn-4/GC-01 (Fig. 2a,e, Fig. 7e-f) showed the presence of titanomagnetite, greigite, and pyrite. In core NGHP-01-15A, titanomagnetite and quartz are two dominant minerals noticed throughout the core (Fig. 7g-l). Few minor peaks of pyrite are seen in Z-II (Fig. 7h), Z-IV (Fig. 7k), and Z-V (Fig. 7l).

#### **4.6. Petrography of authigenic carbonates, chemosynthetic community and sand layers**

Abundant yellowish-brown color authigenic carbonates of different morphologies and sizes are found only in Z-I (upto 1.57 mbsf) of core SSD-45/Stn-4/GC-01 (Fig. 8a-g). Living chemosynthetic communities including *Bathymodiolus* sp., (Fig. 8h), *Calyptogena* sp. (Fig. 8i), *Acharax* sp. shell (Fig.

8j) and Decapod crustaceans (squat lobsters; Fig. 8k) were noticed at the active methane seep site (SSD-45/Stn-4/GC-01). Petrographic thin section analysis of methane-derived authigenic carbonates from shallow gas hydrate (active cold seep) bearing core (SSD-45/Stn-4/GC-01) showed dissolution structure with dominant mineralogy of micritic aragonite, calcite and magnesium calcite (Fig. 9a-b). Bryozoans of circular type structure and its preserved fossils are observed at 1.01 mbsf (Fig. 9c). Foraminiferal tests of different size and shape cast are found in the micritic aragonite (Fig. 9d). Several layers of fine-medium sand were observed in all sediment magnetic zones in core NGHP-01-15A (Fig. S2a-d).

#### **4.7. Rock magnetic properties of shallow (active cold seep) and deep-seated gas hydrate system.**

Based on the rock magnetic properties, we broadly classify the samples into three distinct groupings (Fig. 10a-c). Majority of the samples from shallow hydrate core (SSD-45/Stn-4/GC-01) exhibited both low and intermediate values of  $\chi_{lf}$ , SIRM and SIRM/ $\chi_{lf}$  and showed close groupings (Fig. 10a-b). Samples possessing higher values of SIRM/ $\chi_{lf}$  and comparatively low values of  $\chi_{lf}$  can be attributed to the presence of fine-grained ferri- and paramagnetic iron sulfides (Fig. 10b). Contrastingly, samples from core NGHP-01-15A showed relatively high and intermediate values of  $\chi_{lf}$ , SIRM and SIRM/ $\chi_{lf}$  values indicating the dominance of mixed-type (iron oxides, iron sulfides) mineral assemblages (Fig. 10a-b). A good covariation between concentration dependent ( $\chi_{lf}$ ) and mineralogy diagnostic (S-ratio) is noticed (Fig. 10c). Higher values of  $\chi_{lf}$  coupled with the S-ratio  $> 0.9$  in both the sediment cores can be attributed to the presence of ferrimagnetic (magnetite) particles. Samples from core SSD-45/Stn-4/GC-01 exhibiting low S-ratio showed narrow range in  $\chi_{lf}$  indicating the presence of high coercive ferrimagnetic magnetic minerals (hematite, goethite) or ferrimagnetic iron sulfides (greigite, hexagonal pyrrhotite) (Fig. 10c; Peters and Dekkers, 2003; Roberts et al., 2011; Kars and Kodama, 2015; Horng, 2018). While samples from core NGHP-01-15A which showed low S-ratio exhibited wide range in  $\chi_{lf}$  (Fig. 10c). The day plot showed that all the analyzed samples from shallow and deep-seated gas hydrate sediment cores lie in the vortex state (Fig. 10d; Day et al., 1977).

## **5. Discussion**

### **5.1. Origin of magnetic minerals and its fate in sulfidic and methanic environments.**

Rock magnetic and mineralogical methods provided suitable means to characterize magnetic assemblages in a complex active cold seep and methane-hydrate bearing marine sedimentary system with different sources (detrital, diagenetic, authigenic) of the magnetic particles. It is pre-requisite to evaluate the factors contributing and affecting the magnetic signals for better interpretation of sediment magnetic record in context with primary (detrital) and secondary (diagenetic/authigenic) depositional

processes (Housen and Musgrave, 1996; Roberts, 2015). The sediment magnetism at sites representing shallow (SSD-45/Stn-4/GC-01) and deep-seated (NGHP-01-15A) gas hydrate system is carried by a complicated magnetic mineral assemblages comprised of detrital (titanomagnetite, magnetite, silicate-hosted magnetic inclusions) diagenetic (pyrite), and authigenic (magnetite, greigite) origin as confirmed by rock magnetic, XRD, SEM-EDS and optical microscopy (Fig. 2-7, Fig. 10, Fig. S3, Fig. S4). In the studied sediment cores, the degree of influence of each magnetic mineral phase varied within sulfidic and methanic sedimentary zones as clearly evident in rock magnetic (Fig. 2) and mineralogical records (Fig. 6-7). Detrital magnetic particles occur as discrete vortex state-MD type magnetite (as confirmed through FORC and SEM-EDS; Fig. 5; Fig. 6, Fig. S6) as well as silicate-hosted magnetic inclusions (Fig. S3, Fig. S4) in the both the sediment cores. Higher values of  $\chi_{fr}$  in Z-I of both cores can be attributed to the presence of fine and coarse-grained detrital titanomagnetite mainly sourced from Deccan trap basalts (Fig. 2, Fig. 6-7; Ramesh and Subramanian, 1988; Sangode et al., 2001; Badesab et al., 2019). Thermomagnetic curves ( $\chi$ - $T$ ) confirmed that the bulk magnetic mineralogy is dominated by titanomagnetite including magnetite (Dunlop et al., 1997). The data also showed the dominance of non-magnetic iron phase in samples from both sediment cores (Fig. 3a-b). The thermal transformation at 352°C (SSD-45/Stn-4/GC-01) and 373.5°C (NGHP-01-15A) is consistent with the high temperature oxidation of a non-magnetic iron phase into a magnetic phase (Fig. 3a-b; Passier et al., 2001). The broadness of the oxidation peak in the NGHP-01-15A samples could be attributed to the presence of two different morphologies of pyrite. Similar observations were reported from equatorial Atlantic (Itambi et al., 2010) and Mediterranean sediments (Passier et al., 2000). Mineralogy diagnostic low-temperature magnetic data of core SSD-45/Stn-4/GC-01 revealed no distinct Verwey transition in the topmost sediment interval (Fig. 4a-b) and gas hydrate bearing layers (Fig. 4c-f). Such feature can be reconciled to the masking of transition due to increase in paramagnetic contribution (Verwey, 1947). Rapid loss of LT-SIRM between 5 and 30 k in these samples could be due to increased contribution from SP magnetic particles (Tarduno, 1995) or paramagnetic (e.g., silicates; Itambi et al., 2010). Non-stoichiometry, cation substitution and grain size can also suppress the appearance of the Verwey transition (Kakol et al., 1992; Halgedahl and Jarrard, 1995). Partial oxidation of magnetite followed by an increase in paramagnetic contribution exhibited by diagenetically formed pyrite (Fig. 6b,d-f) at several sediment intervals in core SSD-45/Stn-4/GC-01 might have masked the transition and provide evidence for the claim. Titanomagnetite and SP greigite (Fig. 5; Muxworthy and Dunlop, 2002) particles are found to occur throughout in core SSD-45/Stn-4/GC-01 (Fig. 2a,e, Fig. 6a-f, Fig. S6a-f). Increase in Ti-content (Moskowitz et al., 1998) and presence of SP (Itambi et al., 2010) particles might have also contributed to the masking of the Verwey transition.

Silicate hosted (fine-grained magnetic particles) inclusions were found to be spatially distributed throughout and remain survived through sulfidic, methanic and gas hydrate bearing zones in both the sediment cores (Fig. 2, Fig. S3, Fig. S4). Orange-brownish color coating over the surface of silicate grain is indicative of overgrowth of iron-sulfide previously formed during reductive diagenesis (Fig. S3b-c; Larrasoña et al., 2007; Badesab et al., 2020a). It is clear that the finer magnetic particles occurring as inclusions within the silicate matrix remained protected and survived the reductive diagenetic dissolution and pyritization reactions throughout (Hounslow and Maher, 1996; Hatfield, 2014; Chang et al., 2016). Enrichment of SP particles in sulfidic and methanic environment has been previously linked with the growth of fine-grained ferrimagnetic iron sulfides like greigite (Rowan et al., 2009; Kars et al., 2021). Elevated SIRM/ $\chi_{lf}$  values (Fig. 2e,k) in core SSD-45/Stn-4/GC-01 (0.01–0.35 mbsf, 1.75 – 1.85 mbsf, 2.05 – 2.11 mbsf) and in core NGHP-01-15A (38.86 – 63.97 mbsf) indicates that the presence of authigenic SP greigite (Snowball, 1991; Larrasoña et al., 2007; Blanchet et al., 2009; Loughheed et al., 2012). Similar observations of enhanced SIRM/  $\chi_{lf}$  linked with the presence of authigenic greigite particles were reported from Santa Barbara Basin (Blanchet et al., 2009), North Central Baltic Sea (Reinholdsson et al., 2013), and Atlantic Ocean (Oda and Torii, 2004). Magnetic grain size proxy (ARM/SIRM) has been utilized as a valuable indicator to detect fine-grained magnetic particles in methanic sediments (Dillon and Bleil, 2006; Lin et al., 2021). Higher ARM/SIRM values in both sediment cores can be linked to authigenic formation of magnetite via microbial iron-reduction process (Elmore et al., 1987; Lovely et al., 1987; Phillips et al. 2017; Vigderovich et al., 2019; Lin et al., 2021). Magnetic mineralogy (S-ratio) proxy showed anomalous zones in both sediment cores. Low S-ratio intervals in shallow SSD-45/Stn-4/GC-01 (0.31 to 1.07 mbsf and 1.83 to 2.23 mbsf; Fig. 2f) and deep-seated gas hydrate NGHP-01-15A (22.91 to 36.77 mbsf; Fig. 2l) bearing sediment cores is manifested by low  $\chi_{lf}$  and can be linked with the authigenic formation of ferrimagnetic iron sulfides (greigite, hexagonal pyrrhotite). Such magnetic iron sulfides were probably no longer stable and got quickly transformed into pyrite (Jiang et al., 2001; Kars and Kodama, 2015; Badesab et al., 2017). Lack of distinct peaks of SP greigite particles in mineralogical record (Fig. 7) in both the sediment cores be explained by the fact that the presence of ample ( $Fe^{2+}$ ) and ( $S^{2-}$ ) in the porewater might have promoted pyrite formation without the complete preservation of intermediate ferrimagnetic iron sulfide i.e., greigite (Kao et al., 2004; Reilly et al., 2020).

## **5.2 Constraints on the formation and preservation of diagenetic and authigenic minerals in the shallow and deep-seated gas hydrate sedimentary system.**

The K-G basin represents an ideal natural laboratory with its unique presence of shallow (active cold seep; SSD-45/Stn-4/GC-01; Mazumdar et al., 2019) and deep-seated (NGHP-01-15A; Collett et al.,

2008) gas hydrate systems to elucidate the constraints on the formation and preservation of diagenetic and authigenic minerals in two different diagenetic settings experiencing variable fluid sequence. Diagenetic and authigenic processes linked with methane seepage and hydrate formation/dissociation processes enhances the growth of iron sulfides which induce a detectable magnetic signature in the host sediments (Esteban et al., 2008; Greve et al., 2021). Detailed rock magnetic and mineralogical analyses on the sediment cores complemented by the petrological observations on the authigenic carbonates helped in examining the diagenetic and authigenic processes in the studied cores. We briefly discuss how magnetic minerals responds to such processes prevailing in two different diagenetic settings. At active seeps, sudden shifting of SMTZ fronts due to changing methane flux and rates of sulfate reduction triggered the non-steady state diagenesis involving magnetite dissolution and authigenic formation of ferrimagnetic magnetite and iron sulfide (greigite, hexagonal pyrrhotite) (Larrasoña et al., 2003; Phillips et al., 2017; Roberts, 2015; Lin et al., 2021; Reilly et al., 2020). At active site SSD-45/Stn-4/GC-01, gas hydrates occur as fracture-filling and tube-type within the host sediments (Mazumdar et al., 2019). Gas plumbing system created by fractures efficiently facilitated the upward methane migration from deeper sources (Dewangan et al., 2011; Sriram et al., 2013; Badesab et al., 2020c). In contrast, constant supply of higher methane fluxes from deeper reservoir, occurrence of deep-seated disseminated-type gas hydrates in sand horizons and well-developed SMTZ (Fig. S7) at site NGHP-01-15, favoured the steady-state diagenesis (Collett et al., 2008). The sediment magnetic signal interms of magnetic concentration, grain size and mineralogy in both type of gas hydrate system is strongly constrained by the history of fluid sequence. Progressive loss of detrital magnetic minerals via dissolution and pyrite formation is clearly evident in the upper most parts of both the sediment cores. Within the sulfidic zone (Z-I), the lowest values of  $\chi_{lf}$  are observed where iron oxides have been reduced to paramagnetic pyrite (Fig. 2a,g). Such signature is typically observed in settings with high methane and sulphate or sulphide flux, for example at methane vents at Cascadia Margin (Esteban et al., 2008), southwestern Taiwan (Hornig, 2018), Hikurangi Margin, New Zealand (Kars et al., 2021), Oman and North California margin (Rowan et al., 2009), Argentina continental margin (Garming and Riedinger, 2005), and Rio De Plata, South Atlantic Ocean (Riedinger et al., 2005).

Magnetic grain size diagnostic (ARM/SIRM) proxy has been effectively used to determine the presence of fine-grained authigenic magnetite in methanic sediments (Peters and Dekkers, 2003; Dillon and Bleil, 2006; Lin et al., 2021). Two distinct pattern in ARM/SIRM profile is noticed in cores from the shallow (Fig. 2d) as well as deep-seated (Fig. 2j) gas hydrate system. Initial (0.01 – 0.19 mbsf) decrease in ARM/SIRM in the uppermost sediment intervals of shallow hydrate core (SSD-

45/Stn-4/GC-01) could be attributed to preferential diagenetic dissolution of fine-grained detrital magnetic particles (Fig. 2d; Peters and Dekkers, 2003). Downcore increase in ARM/SIRM from 0.21 to 1.69 mbsf within Z-I can be linked with the authigenic formation of fine-grained magnetite via microbial iron reduction process (Fig. 2d; Karlin et al., 1987; Lovely et al., 1987; Phillips et al., 2017; Vigderovich et al., 2019; Lin et al., 2021). Similar observations linking the rise in ARM/SIRM to the authigenic growth of SD magnetite in methanic were reported from the Bay of Bengal (Gaikwad et al., 2021), Niger deep-sea fan (Dillon and Bleil, 2006), South China Sea (Lin et al., 2021), and Southern Eastern Mediterranean continental shelf (Amiel et al., 2020). A marked shift of decrease of ARM/SIRM in the Z-II from 1.71 to 2.23 mbsf suggest significant reduction in the growth of authigenically formed fine-grained magnetite possibly due to decline in microbial activity coupled to iron-reduction process (Fig. 2d; Lovely et al., 1987; Egger et al., 2015; Phillips et al., 2017; Rodelli et al., 2018; Rodelli et al., 2019; Lin et al., 2021). In deep-seated gas hydrate core NGHP-01-15A, initial reduction in ARM/SIRM from 0.74 – 13.23 mbsf in sulfidic (Z-I) is due to magnetite reduction linked with reductive diagenesis (Fig. 2j). A systematic gradual increase in ARM/SIRM from 14.02 to 25.86 mbsf in sulfidic (Z-I) i.e., just above SMTZ can be attributed to the presence of fine-grained detrital magnetite which survived the dissolution fronts due to rapid burial in the uppermost sediment intervals. A minor downcore rise in ARM/SIRM below the present-day SMTZ (at 31.5 mbsf) followed by a slow gradual increase further till the bottom of the core (i.e., from 32.36 – 196.45 mbsf) suggest increase in growth of fine-grained authigenic magnetite (Fig. 2j; Elmore et al., 1987; Karlin et al., 1987; Phillips et al., 2017; Lin et al., 2021). A similar steady increase of ARM/SIRM in sediment cores from methanic zone of Niger deep-sea fan (Dillon and Bleil, 2006) and Southern Eastern Mediterranean continental shelf (Amiel et al., 2020) was attributed to the gradual authigenic growth of SD-magnetite. A general trend of gradual downcore increase in greigite diagnostic  $SIRM/\chi_{if}$  (Larrasoana et al., 2007) in the methanic zone below present-day gas hydrate interval (i.e, from Z-II to Z-V) suggest increase in authigenic growth of fine-grained (SP) greigite particles (Fig. 2k; Snowball, 1991).

Stable SD authigenic greigite and magnetite linked with AOM has been widely documented within sediments in methanic environments (Musgrave et al., 2006; Enkin et al., 2007; Larrasoana et al., 2007; Kars and Kodama, 2015; Phillips et al., 2017; Shi et al., 2017; Badesab et al., 2019). Rock magnetic and mineralogical records confirmed the presence of authigenic greigite and magnetite in both cores (Fig. 2, Fig. 6, Fig. 7). We make an attempt to elucidate their formative mechanism and underlying controls in the sulfidic and methanic zones. We put forward two scenarios to unravel the mechanism of authigenic formation of magnetite and greigite in shallow and deep-seated gas hydrate system in the Bay of Bengal. At active seep site, sulfate-driven AOM induced by higher methane results in the

formation of authigenic carbonates and iron sulfides at SMTZ (Housen and Musgrave, 1996; Suess, 2014; Liang et al., 2017). Changes in the methane flux might have created SMTZ fronts induced by multiple AOM. Subsequently, hydrogen sulfide produced at SMTZ fronts will cause the dissolution of iron oxides, followed by successive precipitation of iron sulfides (Pulton et al., 2004; Riedinger et al., 2014; Kars and Kodama, 2015; Xie et al., 2019; Greve et al., 2021). Fluctuations in  $\chi_{\text{lf}}$  and occurrence of authigenic carbonates throughout in Z-I provides evidence on the multiple AOM fronts at active seep site (SSD-45/Stn-4). Lin et al (2021) reported that oxidation of iron-sulfides at SMTZ is enhanced during the periods of lower methane seepage and generates secondary iron (oxyhydr) oxides. As methane seepage increases, such iron (oxyhydr) oxide serves as a reactive iron source for magnetite authigenesis linked with microbial iron-reduction resulting in the authigenic formation of magnetite. Previous studies provided rock magnetic and geochemical evidence for authigenic magnetite formation via iron reduction in sediments (IODP Site C0020) offshore Shimokita Peninsula, Japan (Phillips et al., 2017) and eastern equatorial Pacific (Karlin et al., 1987). Overall, high ARM/SIRM and  $\chi_{\text{lf}}$  from 0.21 to 1.69 mbsf in methanic zone (Z-I) of core SSD-45/Stn-4/GC-01 can be attributed to the presence of fine-grained authigenic magnetite and provides compelling evidence on the magnetite authigenesis occurring in this zone probably due to rapid change in diffusive methane fluxes controlled by opening/closing dynamics of underlying fault/fracture system at this site (Fig. 2a,d).

In the methanic zone, AOM seems to be a major biogeochemical process that affects magnetic mineral assemblages in marine sediments (Roberts et al., 2018). Sulfate-reduction via AOM utilizes pore water methane and sulfate to near depletion at the SMTZ and provides a secondary source of hydrogen sulfide (Niewöhner et al., 1998; Kasten and Jørgensen, 2000) that drives reductive dissolution of detrital iron oxides and formation of secondary ferrimagnetic iron sulfides. A marked shift of decrease in  $\chi_{\text{lf}}$  and ARM/SIRM values in methanic zone (Z-II; 1.71 to 2.23 mbsf) of core SSD-45/Stn-4/GC-01 revealed significant decline in the growth of authigenic magnetite (Fig. 2a,d). It is quite possible that either bulk of newly formed authigenic (fine-grained) magnetite were preferentially removed by diagenetic dissolution because of intense AOM itself or decline in methane flux due to hydrate accumulation in Z-II might have not supported the authigenic formation of fine-grained magnetite. Fracture-filled gas hydrates were recovered from Z-II of core SSD-45/Stn-4/GC-01 (Mazumdar et al., 2019). Presence of high reactive iron and limited sulfide concentration rather favoured the formation of authigenic greigite in Z-II of core SSD-45/Stn-4/GC-01. This observation suggests that greigite might have started forming only after hydrate formation in Z-II. High SIRM/ $\chi_{\text{lf}}$  in the gas hydrate bearing sediment intervals in Z-II of core SSD-45/Stn-4/GC-01 confirmed the presence of authigenic greigite (Fig. 2e; Snowball, 1991; Blanchet et al., 2009; Lowgheed et al., 2012). SEM-EDS and XRD



data confirmed the presence of detrital coarse-grained titanomagnetite (which survived dissolution), diagenetic pyrite and authigenic greigite in Z-II (Fig. 6e-f, Fig. S6 e-f, Fig. 7e-f). The sustenance of high methane flux in Z-II of core SSD-45/Stn-4/GC-01 most likely inhibited the oxidation of previously formed diagenetic iron sulfides and constrained the production of reactive iron source needed/required for magnetite authigenesis in Z-II (Elmore et al., 1987; Karlin et al., 1987; Phillips et al., 2017; Lin et al., 2021). A noticeable drop followed by consistent lower ARM/SIRM values reflect significant reduction in the growth of fine-grained authigenic magnetite in the methanic environment (Z-II; 1.69 to 2.23 mbsf) of core SSD-45/Stn-4/GC-01 (Fig. 2d). High SIRM/ $\chi_{lf}$  (0.1 to 0.25 mbsf) in the uppermost sediment interval of Z-I suggests that the interplay between downward migrating sulfate and upward rising methane probably favoured greigite authigenesis just below the near-surface sulfidic zone (Fig. 2e; Kars and Kodama, 2015; Larrasoña et al., 2007). A systematic decrease of SIRM/ $\chi_{lf}$  within Z-I (Fig. 2e) can be attributed to slow conversion of ferrimagnetic greigite to pyrite in Z-I of core SSD-45/Stn-4/GC-01 (Snowball, 1991; Larrasoña et al., 2007; Musgrave et al., 2019). Similar observations were reported from Izu-Bonin rear arc, Japan (Musgrave et al., 2019), Blake Ridge (ODP Site 997; Shipboard Scientific Party, 1996b), Nankai Margin (IODP Site C002; Shi et al., 2017). More recently, Musgrave et al. (2019) suggested that downcore decrease in SIRM/ $\chi_{lf}$  could also be due to the shift in coercivity of the magnetic particles, as fine-grained detrital magnetite gets selectively dissolved downcore due to authigenic formation of SD/SP greigite particles which can exhibit significantly low S-ratio (Peters and Dekkers, 2003; Dillon and Bleil, 2006; Larrasoña et al., 2007; Roberts et al., 2011; Kars and Kodama, 2015; Horng, 2018). A shift in the coercivity of magnetic particles (Fig. 2f) is seen through a broad and distinct interval exhibiting low S-ratio values in Z-I (0.31 to 1.07 mbsf) and Z-II (1.83 to 2.23 mbsf) in core SSD-45/Stn4/GC-01. This observation provide compelling evidence on the authigenic formation of SP greigite in core SSD-45/Stn-4/GC-01 (Fig. 5; Muxworthy and Dunlop, 2002) during magnetite reduction process and validates the interpretation of Musgrave et al. (2019). A magnetic mineral diagenetic study on the sediment core from Perseverance Drift, North-western Weddell Sea by Reilly et al. (2020) made similar observations. They attributed that the high coercivity layers (marked by low S-ratio) below SMTZ in core JKC36 were formed due to porewater transition, where downward diffusing sulfate is limited, but the iron ( $Fe^{2+}$ ) concentration still exist which provided favourable conditions for the growth of greigite and hexagonal 3C pyrrhotite. Greigite is well-known to occur in methane-rich sediments, methane hydrates or in consortium with methane diffusion (Housen and Musgrave, 1996; Musgrave et al., 2006; Larrasoña et al., 2007; Roberts, et al., 2018; Kars et al., 2021). More recently, a high-resolution rock magnetic study on a sediment core from IODP Site U1518 at Hikurangi Margin, offshore New Zealand reported the

formation of authigenic greigite linked to methane diffusion and disseminated-type methane hydrate within sediments (Kars et al., 2021). In methanic zone (Z-II) of core SSD-45/Stn4/GC-01, enhanced microbial activity in the presence of gas hydrates might have favoured the formation and preservation of greigite (Musgrave et al., 2006; Kars et al., 2018, 2021). High SIRM/ $\chi_{lf}$  peaks within three gas hydrate intervals in Z-II of core SSD-45/Stn4/GC-01 support the interpretation (Fig. 2e). Similar observations were reported from Blake Ridge (Wellsbury et al., 2010) and Hydrate Ridge (Larrasoña et al., 2007), Santa Barbara Basin, California (Blanchet et al., 2009), Atlantic Ocean (Oda and Torii, 2004), Baltic Sea (Lowgheed et al., 2012). At active seep site (SSD-45/Stn-4), methane seepage dynamics controlled the precipitation of authigenic carbonates (Mazumdar et al., 2019; Dewangan et al., 2021). Recently Mazumdar et al. (2019) emphasized that high flux of hydrogen sulfide across the sediment–water interface at active cold seep site (SSD-45/Stn-4) supported the existence of AOM close to the sea floor. Abundant occurrence of MDAC (almost in all samples) within Z-I (only) of SSD-45/Stn-4/GC-01 indicate that enhanced methane flux from deeper reservoir triggered multiple and strong AOM's which resulted in the formation of thick carbonate layers. Dissolution structure and cavity (Fig. 9a,b,d) within the carbonates provide convincing evidence on the high methane seepage at this site (Aloisi et al., 2000). Lack of authigenic carbonates in the methanic environment (Z-II) of core SSD-45/Stn-4/GC-01 could be either due to weak AOM caused by decline in the supply of rising methane flux from deeper reservoir, closure of underlying fractures/fault (Gaikwad et al., 2021), or due to hydrate accumulation underneath (Housen and Musgrave, 1996).

In a sediment core (NGHP-01-15A) from the deep-seated gas hydrate system, detrital (discrete and inclusions - titanomagnetite, magnetite), diagenetic (pyrite) and authigenic (magnetite, greigite) minerals of varying concentration and grain size controlled the bulk sediment rock magnetic properties (Fig. 2, Fig. 3, Fig. 6, Fig. 7, Fig. S6). Downcore decline in  $\chi_{lf}$  from the uppermost 0.74 mbsf to 17.76 mbsf in core NGHP-01-15A is linked with preferential loss of fine-grained detrital magnetic particles due to diagenetic dissolution (Roberts, 2015). A sharp increase in  $\chi_{lf}$  (19.86 – 28.07 mbsf) coupled with high ARM/SIRM just above the present-day SMTZ (Fig. S7) in Z-I of core NGHP-01-15A can be reconciled to the presence of fine-grained detrital magnetite which survived the dissolution fronts in the uppermost sediment intervals due to increase sedimentation. A trend of gradual rise in ARM/SIRM downcore from Z-II to Z-V just below present-day SMTZ in core NGHP-01-15A can be reconciled with the slow growth of authigenic magnetite in these zones (Fig. 2j, Fig. S7; Elmore et al., 1987; Lovely et al., 1987; Karlin et al., 1987; Phillips et al., 2017; Vigderovich et al., 2019; Lin et al., 2021). The mineralogy of authigenic carbonate in core NGHP-01-15A is mainly composed of Fe-rich carbonate mineral with minor amount of low-magnesium calcite (LMC) (Teichert et al., 2014). Deep-

sourced fluid and gas migration generated high gas hydrate saturations within the sand-rich sediment interval at site NGHP-01-15 (Collet et al., 2008; Riedel et al., 2011). Similarly, several sand layers were also found to occur in different sediment intervals (15.83 mbsf to 192.48 mbsf, Fig. 2, Fig. S2; Table. 3; Collett et al., 2008) in core NGHP-01-15A. A comprehensive pore-water geochemical and isotope ratio study in core NGHP-01-15A revealed that the carbon dioxide (CO<sub>2</sub>) produced through microbial methanogenesis got effectively neutralized by silicate weathering. This process resulted in generation of excess alkalinity which got further sequestered in Ca and Fe-carbonates (Solomon et al. 2014; Teichert et al., 2014). The mineral composition of authigenic carbonates suggest that formation of Fe-rich carbonates in core NGHP-01-15A are predominantly related to the silicate weathering reactions coupled to microbial methanogenesis (Solomon et al., 2014; Torres et al., 2020). We propose that a highly porous environment created by several layers of coarse-grained sand and discrete authigenic carbonates might have facilitated the efficient percolation of downward diffusing oxidizing fluids, which preferentially favoured iron sulfide oxidation. This led to the subsequent generation of secondary iron (oxyhydr) oxides required for authigenic formation of magnetite via microbial iron-reduction process in methanic zone in core NGHP-01-15A (Elmore et al., 1987; Lovely et al., 1987; Karlin et al., 1987; Phillips et al., 2017; Vigderovich et al., 2019; Lin et al., 2021). Similar to our observations, microbial iron-reduction in the methanic zone of SE Mediterranean continental shelf (Vigderovich et al., 2019) and Bothnian Sea sediments (Egger et al., 2015) was unravelled based on the geochemical pore water profiles and isotopic records. A gradual rise in ARM/SIRM from Z-II to Z-V in core NGHP-01-15A reflect the slow growth of authigenic magnetite and provide support to our hypothesis (Fig. 2j).

In core NGHP-01-15A, two trends of rise in SIRM/ $\chi_{lf}$  from 38.86 to 63.97 mbsf (uppermost- below SMTZ) and 91.85 to 196.45 mbsf (lowermost- gas hydrate and methanic zone) confirmed the presence of authigenic greigite in Z-III, Z-IV, and Z-V (Fig. 2k; Snowball, 1991; Tarduno, 1995; Larrasoana et al., 2007). Two scenarios have been proposed to explain the authigenic growth of greigite below SMTZ (Fig.11). High concentration of hydrogen sulfide produced at the present-day SMTZ front might have been completely utilized during pyritization as seen through distinct minima in  $\chi_{lf}$  just below SMTZ (Fig. 2g, Fig. S7). Consequently, sulfide deficient zone was created in the deeper sediment intervals below SMTZ which led to the formation and preservation of greigite (Badesab et al., 2020c). Reduction in rising methane flux due to hydrate accumulation in the underlying sediments might have constrained the sulfide production and preferentially favoured greigite formation and preservation above the present-day gas hydrate occurrence zone (~ 75 - 91 mbsf) in this core. We do not completely rule out the possibility that SP greigite particles (as marked by high SIRM/ $\chi_{lf}$  from 38.86 mbsf to 63.97 mbsf;

Fig. 2k) observed below the present-day SMTZ represent the previously formed greigite particles near the base of the paleo-SMTZ position, when the favourable porewater conditions supported their formation. Late greigite formation linked with deeper diagenetic processes such as gas hydrate formation and AOM has been reported from Neogene marine sediments from New Zealand (Rowan and Roberts, 2006, 2008), North-western Weddell Sea (Reilly et al., 2020) and Nankai Trough (Kars and Kodama, 2015). The gas hydrate occurrence (~ 75 to 81 mbsf; Collett et al., 2008) zone in core NGHP-01-15A lies just below the upper most greigite interval (38.86 mbsf to 63.97 mbsf; Fig. 2k). The sulfide deficient zone created by weakened AOM might have supported the greigite formation and preservation in these intervals. We propose that weakened AOM could be attributed to decline in methane flux either because of reduction in supply of rising methane flux from deeper reservoir or due to trapping during hydrate crystallization underneath (Housen and Musgrave, 1996). More recent magnetic study on sediments from Pāpaku fault, Hikurangi Subduction Margin, New Zealand reported that pyritization of authigenic greigite can produced different generations of pyrite formed during late diagenesis in methanic zone (Greve et al., 2021). Absence of greigite in SEM-EDS and XRD data of Z-II and Z-III of core NGHP-01-15A can be explained by the fact that ferrimagnetic authigenic greigite which was formed earlier might have got converted into more stable pyrite (Fig. 6, Fig. 7; Fig. S6; Jiang et al., 2001; Kao et al., 2004; Larrasoña et al., 2007; Kars and Kodama, 2015; Badesab et al., 2017).

A rock magnetic study on hydrate-bearing sediments of the Hikurangi Margin, New Zealand by Kars et al. (2021) suggested that hydrate dissociation could also result in the secondary diagenesis of previously formed greigite to pyrite. In similar lines, Badesab et al. (2020b) identified two magnetic iron sulfide bearing sediment intervals below SMTZ representing the fossil (disseminated-type) gas hydrate zones in core NGHP-01-14A (proximal to core NGHP-01-15A; present study) from the K-G basin. They linked iron-sulfide formation to the microbially-mediated diagenetic reactions fuelled by the presence of gas hydrates. Dedicated rock magnetic studies dealing with authigenesis of magnetic minerals in the gas hydrate-bearing sediments in the Nankai Trough, offshore Japan (Kars and Kodama, 2015) and Cascadia Margin, offshore Oregon (Larrasoña et al., 2007) also identified the fossil gas hydrate horizons based on magnetic proxy ( $SIRM/\chi_{lf}$ ) and pore water anomalies. We propose that high  $SIRM/\chi_{lf}$  interval (38.86 to 63.97 mbsf) above the present-day gas hydrate occurrence zone (Fig. 2k) in core NGHP-01-15A represent the fossil gas hydrate interval considering the fact that slow diffusion of methane after dissociation might have enhanced the microbial activity and favoured insitu formation of ferrimagnetic iron sulfides (greigite). Below the gas hydrate layer, a gradual downcore rise in  $SIRM/\chi_{lf}$  i.e. from Z-III to Z-V (Fig. 2k) of core NGHP-01-15A suggest the presence of fine-

grained authigenic greigite (Fig. 2k; Snowball, 1991). It is highly possible that gas hydrate layer above (~ 75 to 81 mbsf) might have restricted the flow of downward moving oxidising fluid required for the pyritization process and favoured the gradual growth of authigenic greigite in Z-III to Z-V of core NGHP-01-15A (Fig. 2k, Fig. 11; Kao et al., 2004; Luff et al., 2005; Badesab et al., 2020a; Lin et al., 2021; Gaikwad et al., 2021). In Z-IV, high magnetic susceptibility interval (112.85 – 140.35 mbsf) in core NGHP-01-15A is manifested by the presence of coarse-grained detrital titanomagnetite particles supplied during higher sedimentation events and subsequently survived the diagenetic dissolution fronts due to rapid deposition and burial, thereby creating a magnetite-rich sediment interval (Fig. 2g, Fig. S1; Esteban et al., 2008; Kumar et al., 2014; Shankar et al., 2014; Badesab et al., 2019). A magnetically enhanced and laterally extensive band representing several rapid sedimentation events is clearly evident in the sediment magnetic record (Fig. S1; Shanmugam et al., 2009; Shankar and Riedel, 2010; Dewangan et al., 2011; Ramprasad et al., 2011; Krishna et al., 2016; Badesab et al., 2019). A noticeable increase in  $\chi_{if}$  and minor rise in SIRM/ $\chi_{if}$  below the high sedimentation rate interval i.e., from 149.95 mbsf to 196.45 mbsf is indicative of presence of ferrimagnetic greigite (Fig. 2g,k). Numerical simulation study on Nyegga pockmark field (Karsten et al., 2018) and geochemical modelling (Riedinger et al., 2005) of diagenetic processes on continental margin sediment off Argentina and Uruguay revealed that rapid changes in sedimentation can strongly impact the gas hydrate systems by affecting fluid flow and gas seepage activity, authigenic carbonate formation and magnetic mineral diagenesis. One could imagine that increased supply of reactive iron during rapid sediment deposition events in the K-G basin might have significantly altered the pyritization process and rather favoured the greigite formation and preservation (Riedinger et al., 2005; Badesab et al., 2019; João et al., 2021). Authigenic carbonate were mostly found to occur below the present-day SMTZ i.e., from 47.2 to 195.2 mbsf (Fig. 2, Fig. S7, Table. 2). Geochemical data indicate that the present-day SMTZ at this site (NGHP-01-15) is at 31.5 mbsf (Fig. S7; Collet et al., 2008). Lack of authigenic carbonates above SMTZ at this site could be attributed to decline in alkalinity production (Z-I; Solomon et al., 2014) either due to reduction in silicate weathering process driven by microbial methanogenesis (Aloisi et al., 2004; Wallmann et al., 2008; Torres et al., 2020) or weakened AOM constrained by decline in methane flux rising from deeper sources and/or hydrate accumulation underneath.

## 6. Conclusions

Sediment cores SSD-45/Stn-4/GC-01 and NGHP-01-15A provided records of magnetic mineral diagenesis and authigenesis in a shallow (active cold seep) and deep-seated gas hydrate system from the Bay of Bengal. The findings are summarized below:

(i) Detailed rock magnetic measurements complemented by mineralogical and petrological observation on sediment samples revealed that titanomagnetite (detrital) is the dominant magnetic mineral along with diagenetic (pyrite), authigenic (magnetite, greigite) minerals in both sediment cores. Coarse-grained detrital titanomagnetite particles survived diagenetic dissolution along with silicate-hosted fine-grained magnetic inclusions that protected the magnetic particles from sulfidic pore fluids.

(ii) Magnetogranulometric proxies (ARM/SIRM and SIRM/ $\chi_{lf}$ ) provided useful insights on the diagenetic dissolution and authigenic formation of magnetic minerals in the sulfidic, methanic and gas hydrate bearing zones. Rock magnetic data revealed that authigenic magnetite formation within methanic zones of both the cores was linked with microbial iron-reduction process.

(iii) A close linkage between presence of authigenic greigite and fracture-filled gas hydrates in Z-II of shallow hydrate core (SSD-45/Stn-4/GC-01) demonstrate that the greigite formation is governed by the microbially-mediated diagenetic reactions fuelled by the presence of gas hydrates in this zone. In deep-seated gas hydrate core (NGHP-01-15A), greigite bearing sediment intervals (marked by high SIRM/ $\chi_{lf}$  and  $\chi_{lf}$ ) just below the present-day gas hydrate occurrence zone probably reflect the fossil gas-hydrate (disseminated-type) horizons at this site. Multiple occurrences of discrete authigenic carbonate throughout the sulfidic and methanic zones provided evidence on the episodic intensification of AOM at active seep and silicate weathering coupled to microbial methanogenesis at deep-seated gas hydrate site respectively.

(iv) Present work is the first systematic rock magnetic study which makes a new observation on how magnetic minerals respond to the geochemical environment at two different diagenetic settings experiencing variable fluid sequence controlled by shale-tectonism in the Bay of Bengal. Our findings are summarized into a conceptual model (Fig. 11) explaining the constraints on the formation and preservation of diagenetic and authigenic minerals in two different diagenetic systems. Future work integrating rock magnetism, geochemistry and microbiology is required to gain deeper insights into the mechanism by which microbial activity linked to AOM control the magnetite and greigite authigenesis.

## **Acknowledgments**

We thank Director, CSIR–NIO, Secretary MOES, and National Gas Hydrate Program (NGHP) for supporting this study. We acknowledge the support of Dr. Pawan Dewangan (Chief Scientist) and participants of scientific cruise SSD-045 onboard research vessel R/V Sindhu Sadhana of CSIR-NIO, ship cell team and crews onboard for providing assistance in collection of sediment cores and sampling.

T. Ramprasad is thanked for his support. We thank Dr. Abhishek Saha for providing support with petrological analyses. Director of the Centre for Advanced Marine Core Research (CMCR), Kochi University, Japan is thanked for allowing access to the Paleomagnetic laboratory during a research visit of FB as a part of INSA-JSPS fellowship. Dr. Myriam Kars is thanked for providing timely support to FB during the fellowship period at CMCR. Specialized magnetic measurements were conducted at CMCR with the support of DST-JSPS under the scheme JSPS Postdoctoral Fellowship for Overseas Researchers (Strategic Program; JSPS grant GR 17202) and Establishment of Young Researcher Fellowship Program 2017–2018 (IA/Indo-Japanese/F-1/2018) scheme awarded to FB. We thank Chisa Nishimori for providing technical and laboratory support in Kochi. We thank Girish Prabhu, Areef Sardar, Kaveri Salunke, and Prem Piyush Panda for their support in carrying out magnetic and mineralogical analyses. This is CSIR-NIO publication no. XXXX.

Figures:

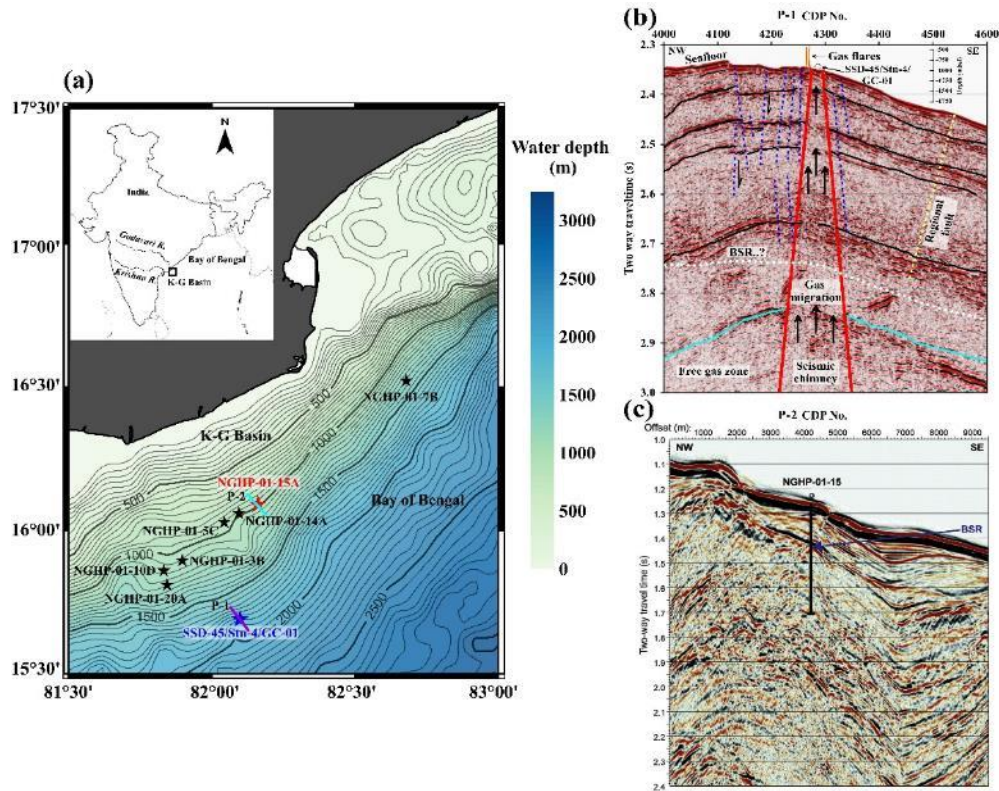


**Fig. 1:** (a) Map showing the sediment core location of shallow (active seep, Core ID: SSD-45/Stn-4/GC-01, marked by red star) and deep-seated (Core ID: NGHP-01-15A, marked by blue star) gas hydrate site. The location of proximal and distal sediment cores (NGHP-01-20A, NGHP-01-10D, NGHP-01-3B, NGHP-01-5C, NGHP-01-14A, NGHP-01-15A, and NGHP-01-7B) collected during National Gas Hydrate Expedition -01 (modified from *Collett et al., 2014*) from the Krishna-Godavari (K-G) basin, Bay of Bengal are shown. High resolution seismic profile of active seep site (SSD-45/Stn-4/GC-01) (P-1) is highlighted in purple color and deep-seated gas hydrate site (NGHP-01-15A) (P-2) is highlighted in light blue color (b) High resolution seismic profile highlighting the normal faults (green dashed lines), subsurface chimney like feature (solid blue lines) and gas flares (purple). Regional toe-thrust fault (yellow dashed line), feasible BSR (white dashed line), and subsurface horizons (solid black lines) are marked on the seismic section from active cold seep location (Core ID: SSD-45/Stn-4/GC-01) (modified from *Dewangan et al., 2021*) (c) High resolution seismic profile of site NGHP-01-15 highlighting the sediment core location and bottom simulating reflector (BSR) with blue color arrow (modified from *Kumar et al. 2014*).



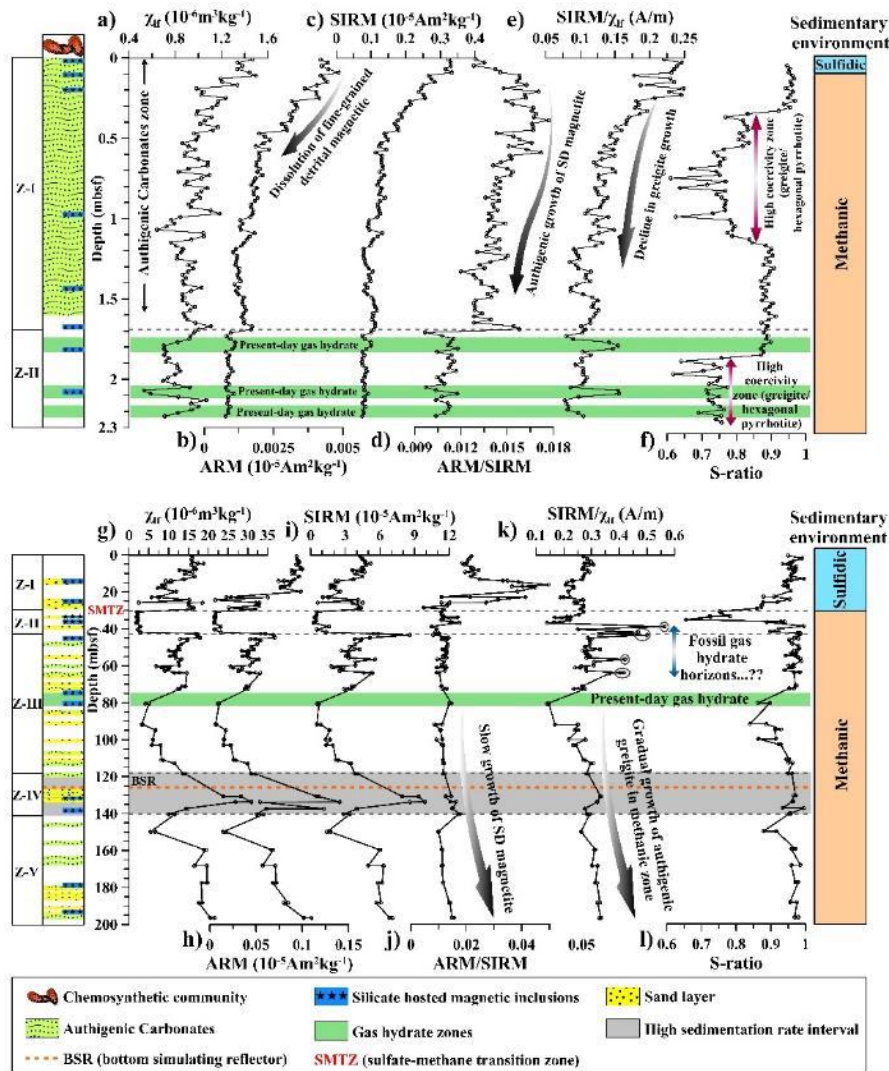


**Fig. 2:** Depth variations of selected rock magnetic data for sediment cores (a–f) shallow (active cold seep, Core ID: SSD-45/Stn-4/GC-01), and (g–l) deep-seated (Core ID: NGHP-01-15A) gas hydrate site. Based on the variation in magnetic susceptibility ( $\chi_{lf}$ ), two sediment magnetic zones (Z-I, Z-II) of shallow (active cold seep) and five sediment magnetic zones (Z-I, Z-II, Z-III, Z-IV, Z-V) of deep-seated gas hydrate site in the Krishna-Godavari (K-G) basin, Bay of Bengal are marked. (Please note that  $\chi_{lf}$  = low frequency magnetic susceptibility; ARM = anhysteretic remanent magnetization; and SIRM = isothermal remanent magnetization).

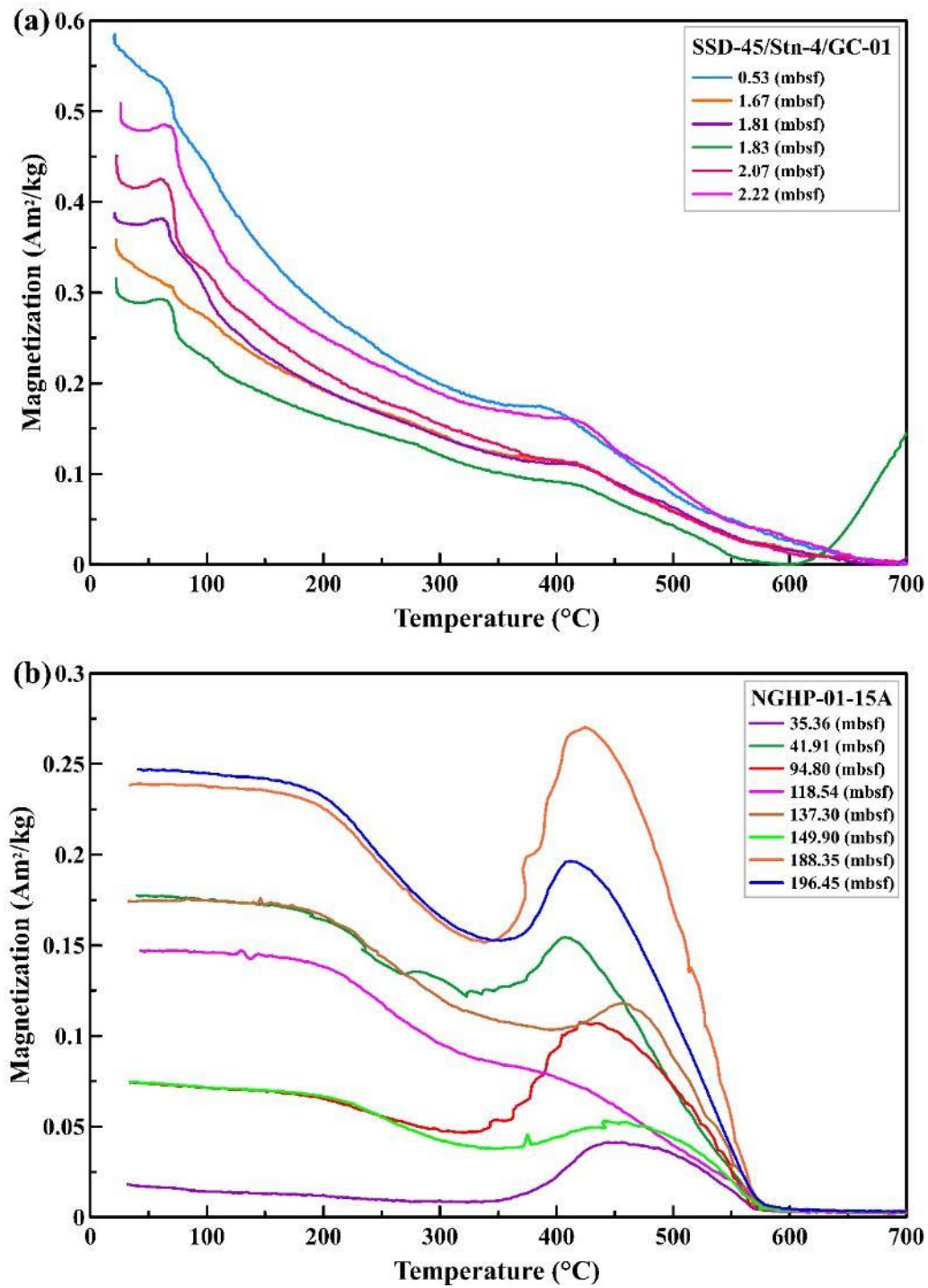


**Fig. 3:** Thermomagnetic heating curves ( $\chi$ - $T$ ) for selected samples from sediment cores (a) shallow (active cold seep, Core ID: SSD-45/Stn-4/GC-01) and (b) deep-seated (Core ID: NGHP-01-15A) gas hydrate site in the Krishna-Godavari (K-G) basin, Bay of Bengal.

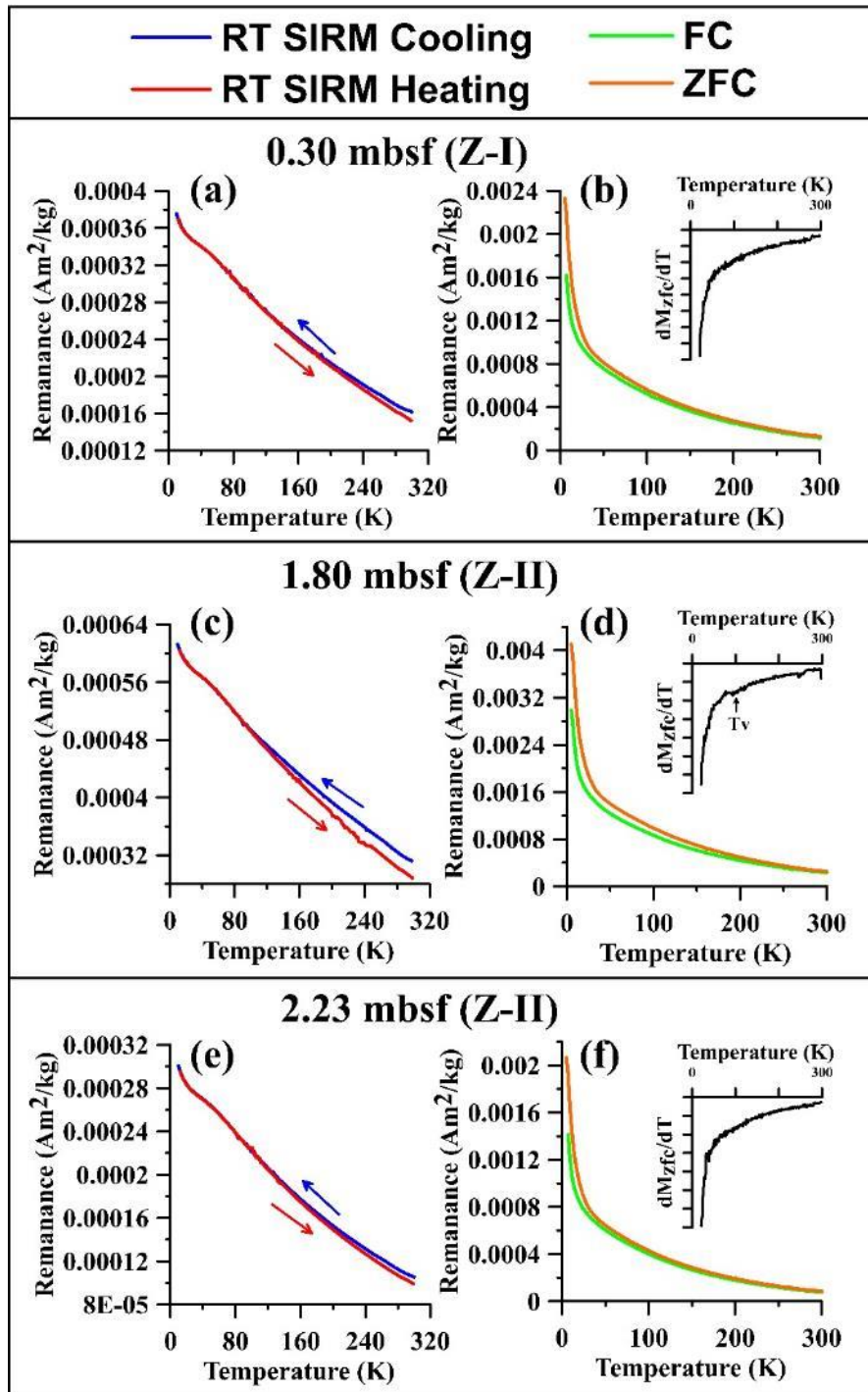


**Fig. 4:** Low-temperature (<300 K) magnetization curves (a–f) for representative samples from the two sedimentary magnetic zones identified in the shallow (active cold seep) gas hydrate core (Core ID: SSD-45/Stn-4/GC-01) in the Krishna-Godavari (K-G) basin, Bay of Bengal (Please note that, FC = field-cooled; RTSIRM = saturation isothermal remanent magnetization at room temperature; ZFC = zero field-cooled).

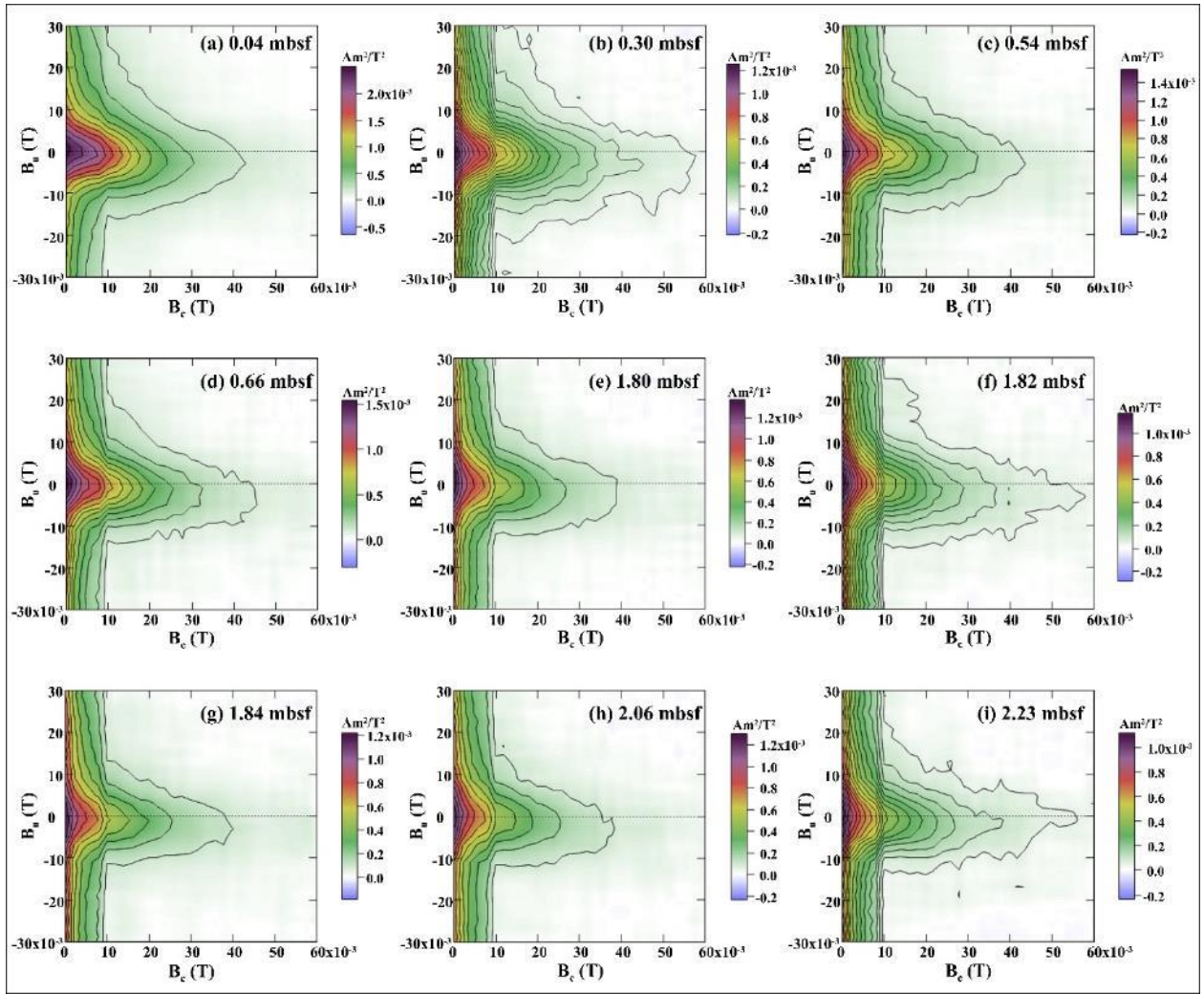


**Fig. 5:** First-order reversal curve (FORC) diagrams (a–i) for selected representative samples from the sediment core (Core ID: SSD-45/Stn-4/GC-01) from shallow (active cold seep) gas hydrate site in the Krishna-Godavari (K-G) basin, Bay of Bengal.

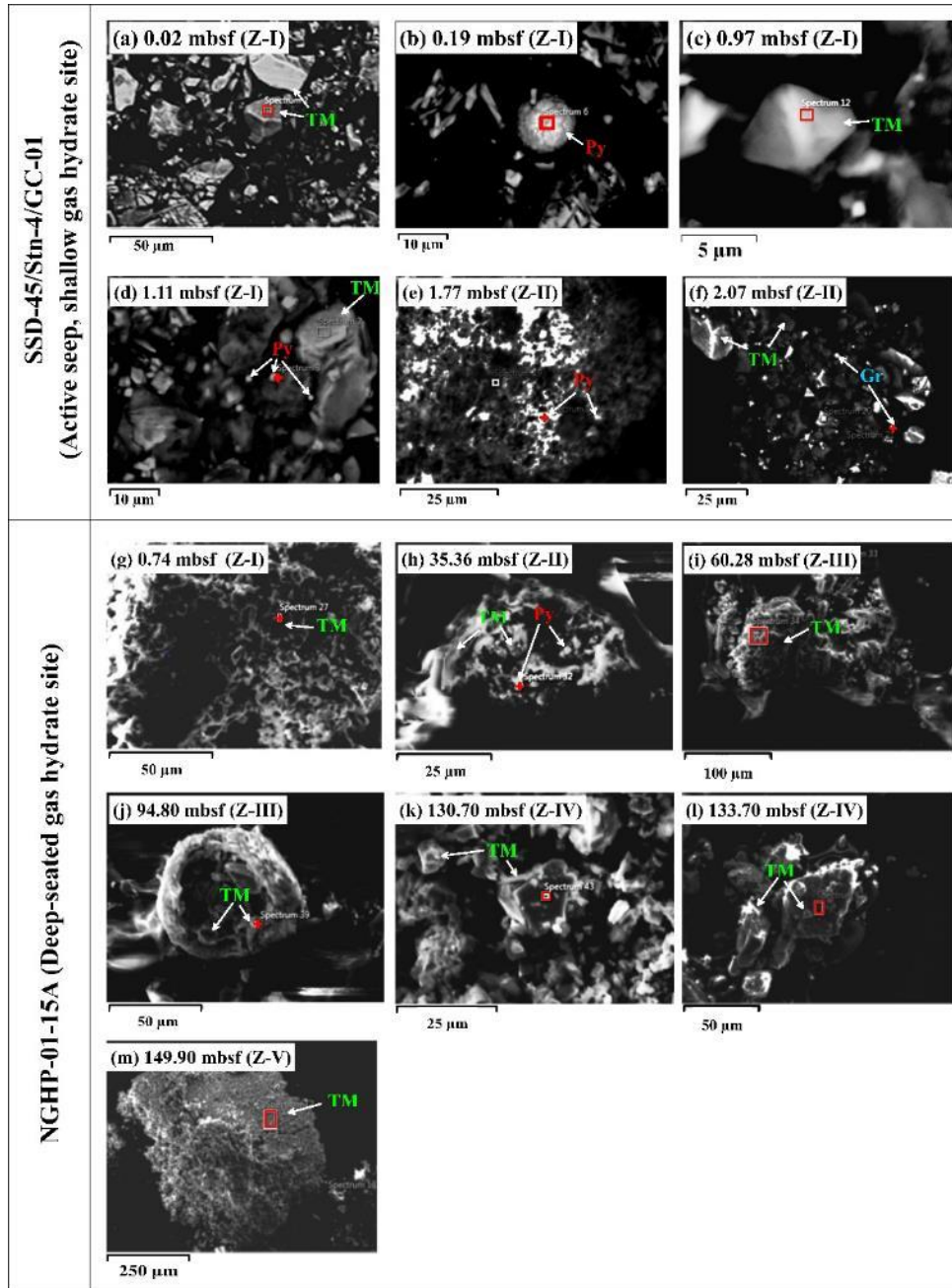


**Fig. 6:** Scanning electron microscope (SEM) images on magnetic extracts from different sediment magnetic zones of cores (a–f) from shallow (active cold seep, Core ID: SSD-45/Stn-4/GC-01) and (g–m) deep-seated (Core ID: NGHP-01-15A) gas hydrate site in the Krishna-Godavari (K-G) basin, Bay of Bengal. Energy dispersive X-ray spectroscopy (EDS) spectra of the respective images presented in the supplementary Fig. S6. Iron (Fe), titanium (Ti), sulfur (S), oxygen (O), calcium (Ca), silicon (Si), carbon (C), aluminium (Al), magnesium (Mg), potassium (K), and vanadium (V) peaks are indicated.

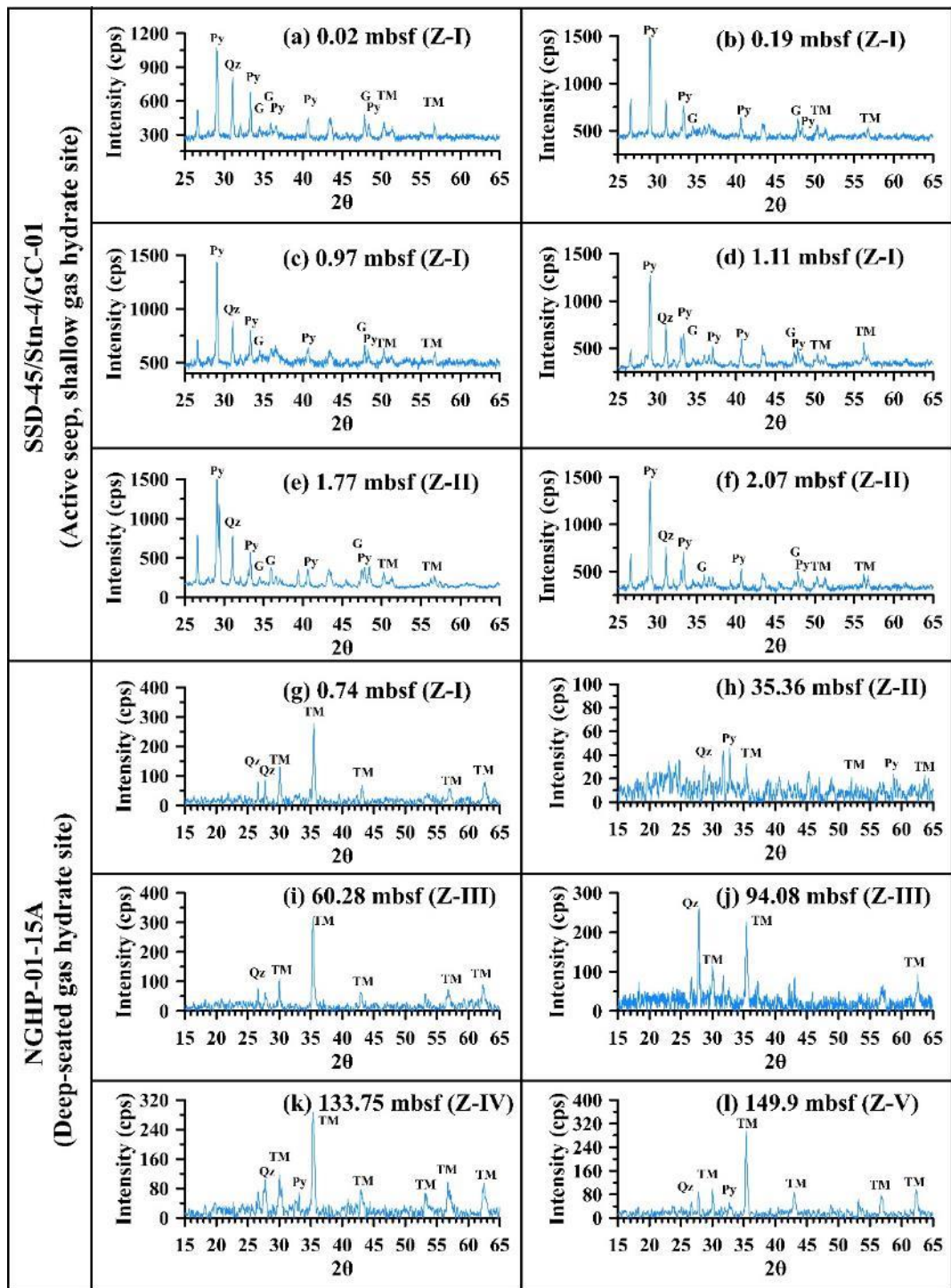


**Fig. 7:** X-ray diffraction spectra for extracted minerals from different sediment zones of cores (a–f) from shallow (active cold seep, Core ID: SSD-45/Stn-4/GC-01) and (g–l) deep-seated (Core ID: NGHP-01-15A) gas hydrate site in the Krishna-Godavari (K-G) basin, Bay of Bengal. TM = titanomagnetite, G = greigite, Py = pyrite, Qz = quartz.

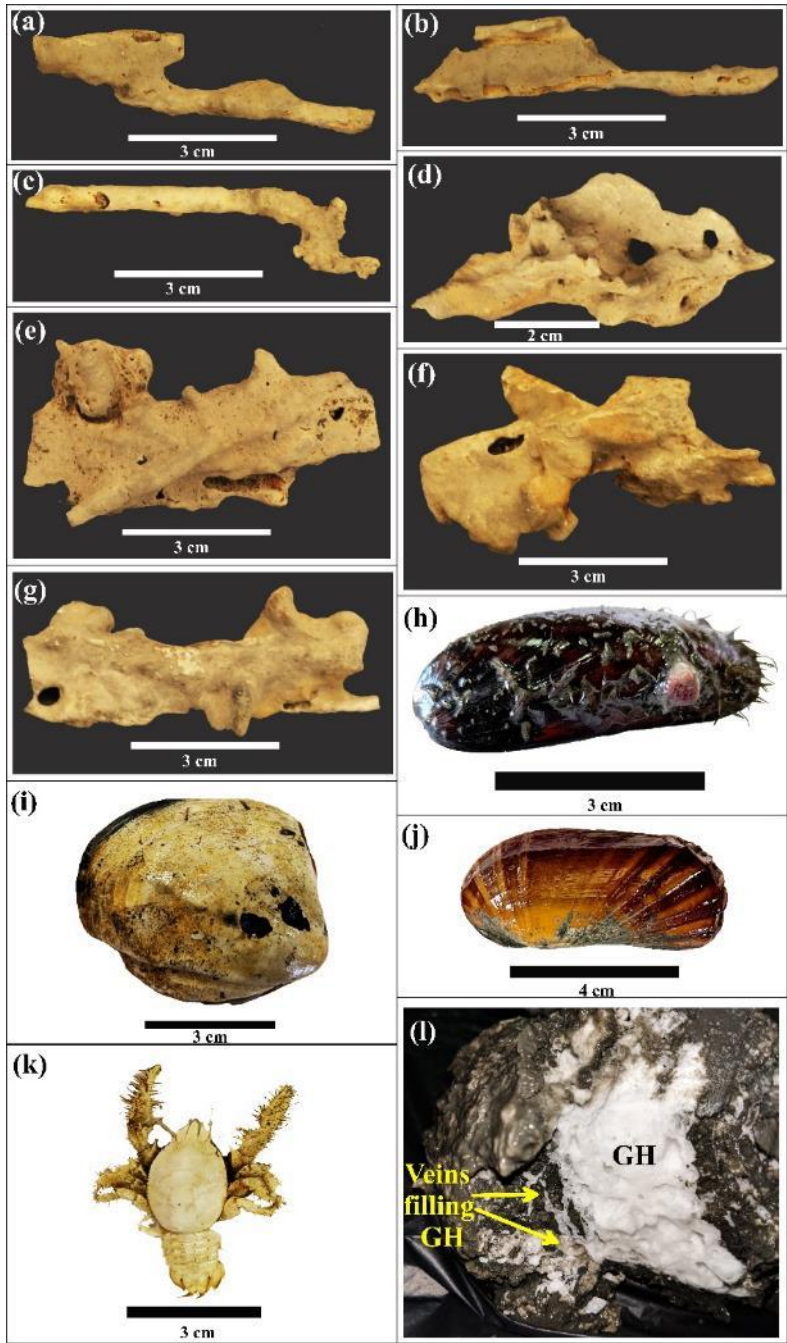


**Fig. 8:** Photographs showing methane-derived authigenic carbonates from different depth intervals of shallow (active cold seep, Core ID: SSD45/Stn-4/GC-01) gas hydrate core: Z-I (a) 0.02 mbsf, (b) 0.18 mbsf, (c) 0.25 mbsf, (d) 0.77 mbsf, (e) 1.01 mbsf, (f) 1.25 mbsf, (g) 1.57 mbsf, chemosynthetic communities from sea floor (h) *Bathymodiolus* Sp., (i) *Calyptogena* Sp., (j) *Acharax* Sp., (k) Decapod crustaceans (Squat lobster), and (l) fracture (vein) filled gas hydrates (2.23 mbsf) recovered from active cold seep site in the Krishna-Godavari (K-G) basin, Bay of Bengal.

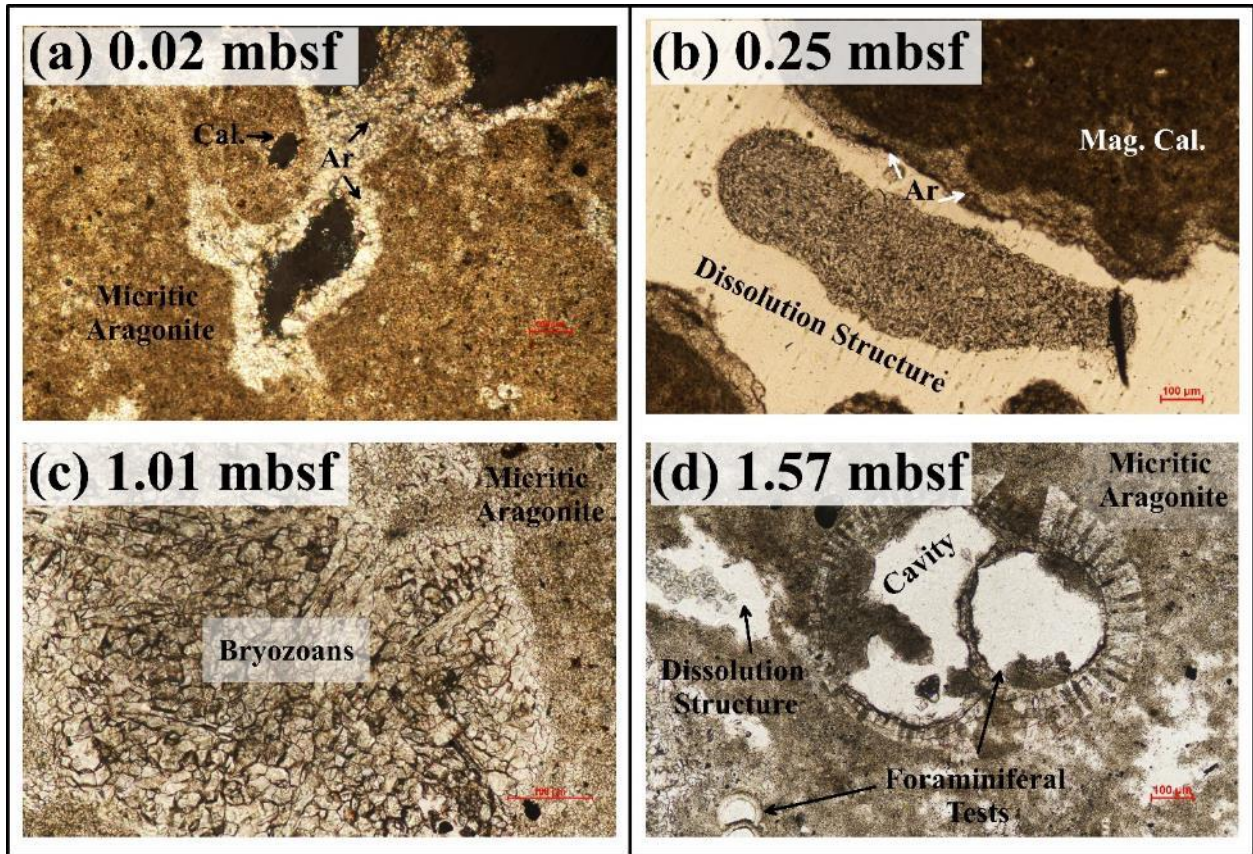


**Fig. 9:** (a–d) Petrographic thin sections of methane-derived authigenic carbonates from shallow (active cold seep, Core ID: SSD-45/Stn-4/GC-01) gas hydrate site in the Krishna-Godavari (K-G) basin, Bay of Bengal. The thin sections were observed under plane-polarized light (Please note that arrow used to highlight the structures and mineral types).



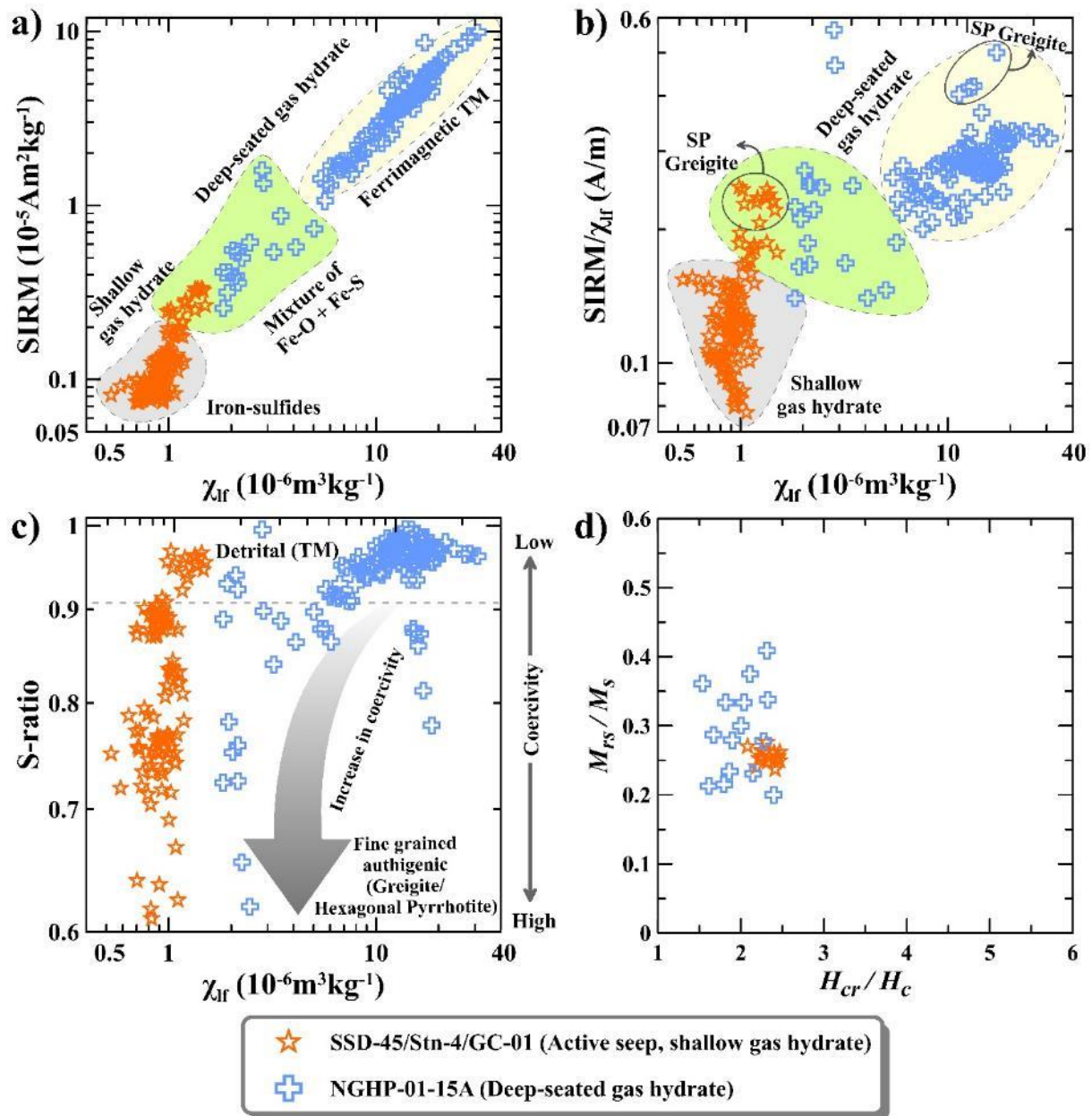
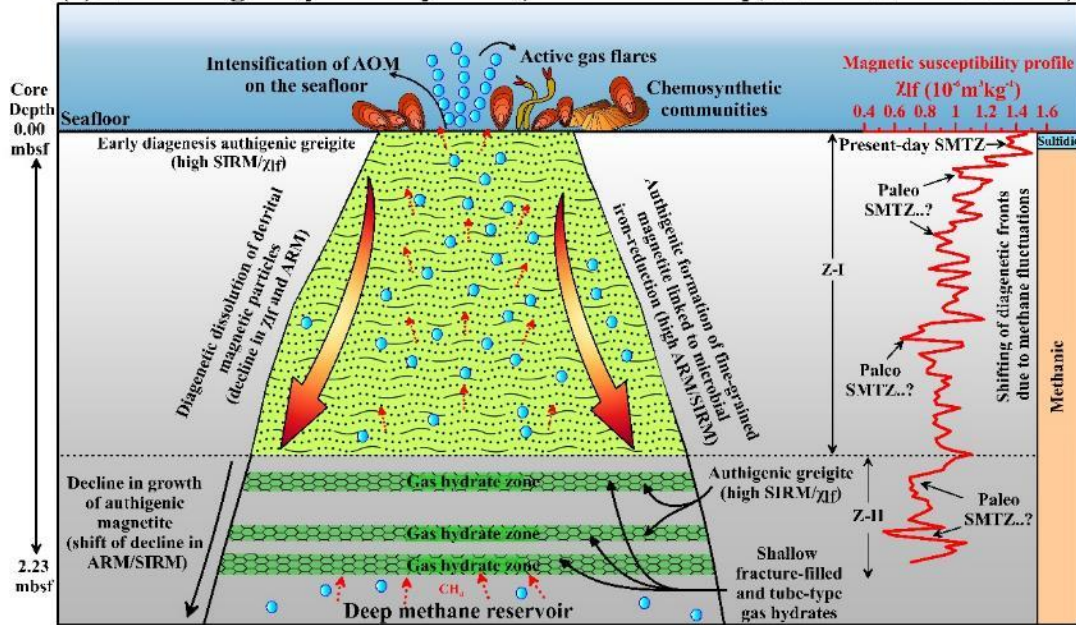


**Fig. 10:** (a–c) Bivariate scatter plots of magnetic parameters: magnetic susceptibility ( $\chi_{lf}$ ), saturation isothermal remanent magnetization (SIRM), SIRM/ $\chi_{lf}$ , S-ratio, and (d) Day plot for samples from shallow (active cold seep, Core ID: SSD-45/Stn-4/GC-01) and deep-seated gas (Core ID: NGHP-01-15A) hydrate site in the Krishna-Godavari (K-G) basin, Bay of Bengal. (Please note that the gray arrow is used in plot (c) to highlight the trend).

**(a) Shallow gas hydrate system (Active cold seep, SSD45/Stn-4/GC-01)**



**(b) Deep-seated gas hydrate system (NGHP-01-15A)**

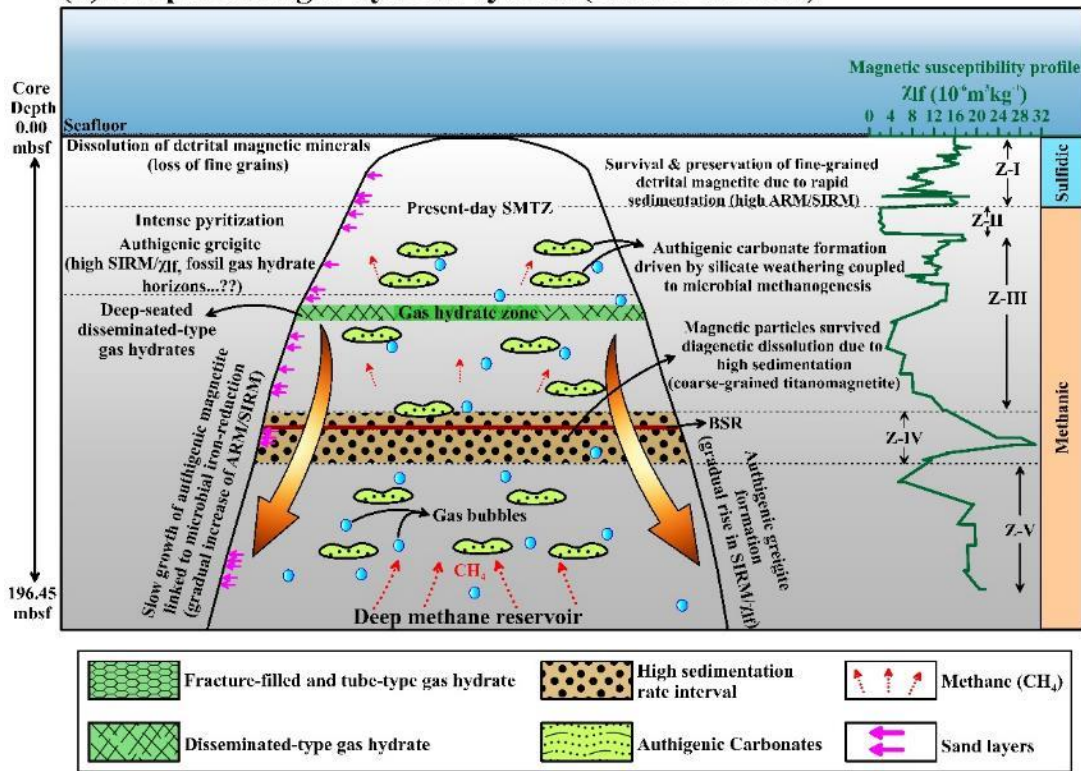


**Fig. 11:** Conceptual model explaining the diagenetic and authigenic controls on the evolution of magnetic mineralogies at (a) shallow (active cold seep, Core ID: SSD-45/Stn-4/GC-01) and (b) deep-seated (Core ID: NGHP-01-15A) in the Krishna-Godavari (K-G) basin, Bay of Bengal.

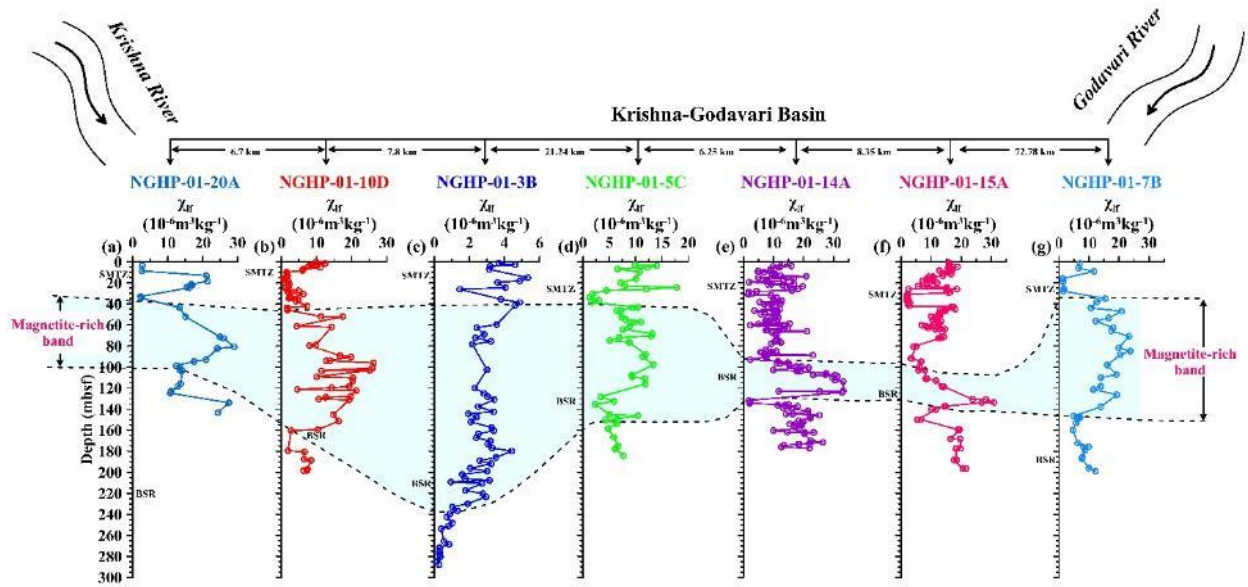


**Fig. S1:** (a-g) Downcore variations of magnetic susceptibility ( $\chi_f$ ) in the sediment cores (NGHP-01-20A, NGHP-01-10D, NGHP-01-03B, NGHP-01-05C, NGHP-01-14A, NGHP-01-15A, and NGHP-01-07B) from the Krishna-Godavari (K-G) basin, Bay of Bengal. Enhanced  $\chi_f$  is highlighted by a color (light blue) band. The distance between the core locations, depth of the bottom simulating reflector (BSR) and the position of the sulfate-methane transition zone (SMTZ) are also marked. (Magnetic susceptibility plots of core NGHP-01-20A is modified from *Badesab et al., 2022*, NGHP-01-10D is modified from *Badesab et al., 2017*, NGHP-01-3B, NGHP-01-5C and NGHP-01-7B are modified from *Badesab et al., 2019*, and NGHP-01-14A is modified from *Badesab et al., 2020b*).

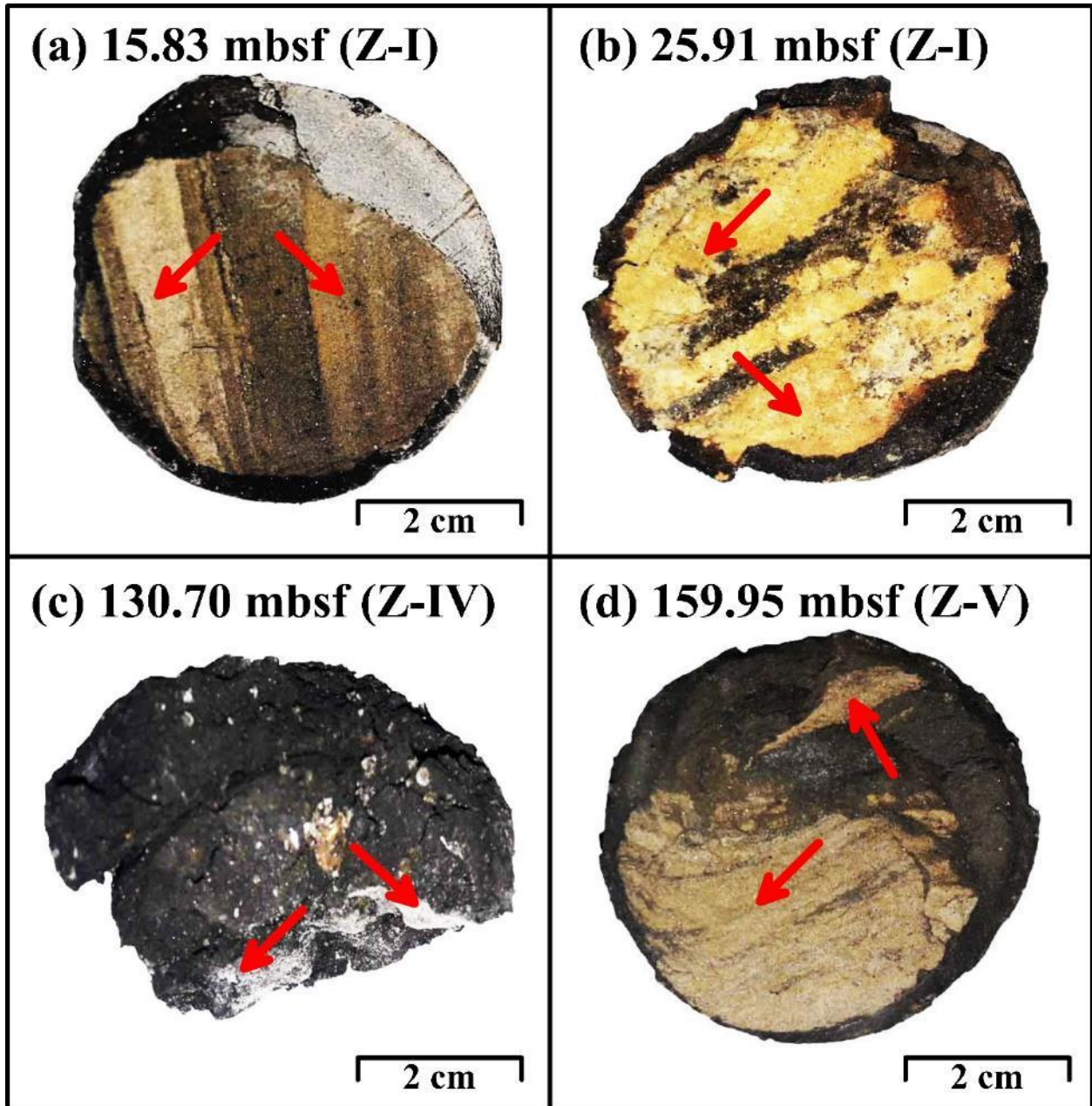


**Fig. S2:** (a-d) Photograph showing fine to medium grained sand layers from different sediment magnetic zones of a deep-seated (Core ID: NGHP-01-15A) gas hydrate site in the Krishna-Godavari (K-G) basin, Bay of Bengal.

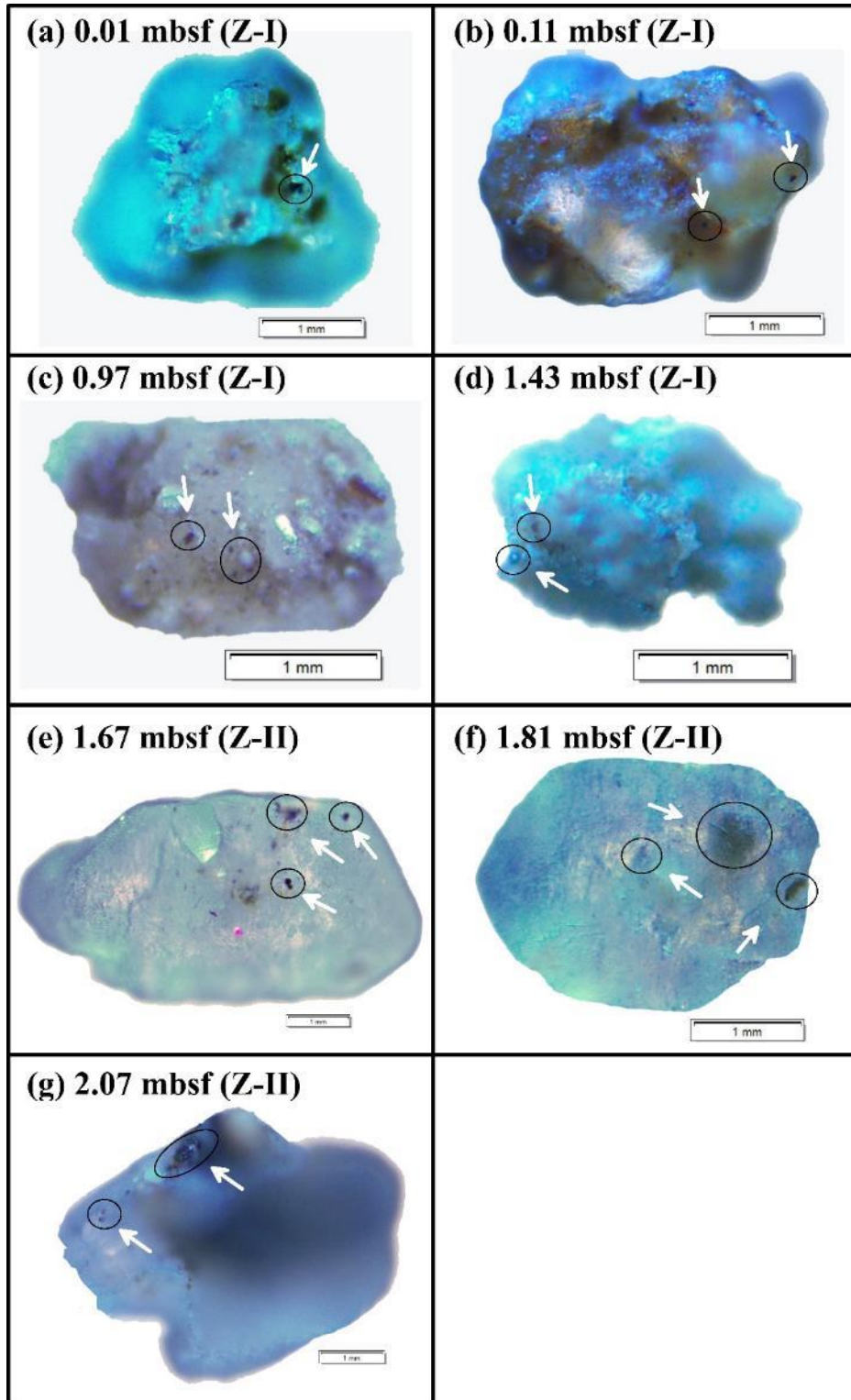


**Fig. S3:** (a–g) Optical microscopic images of the representative (>63 μm) fraction from shallow (active cold seep; Core ID: SSD-45/Stn-4/GC-01). Magnetic inclusion within host quartz (>63 μm) fractions are marked (see black circles and white arrows).

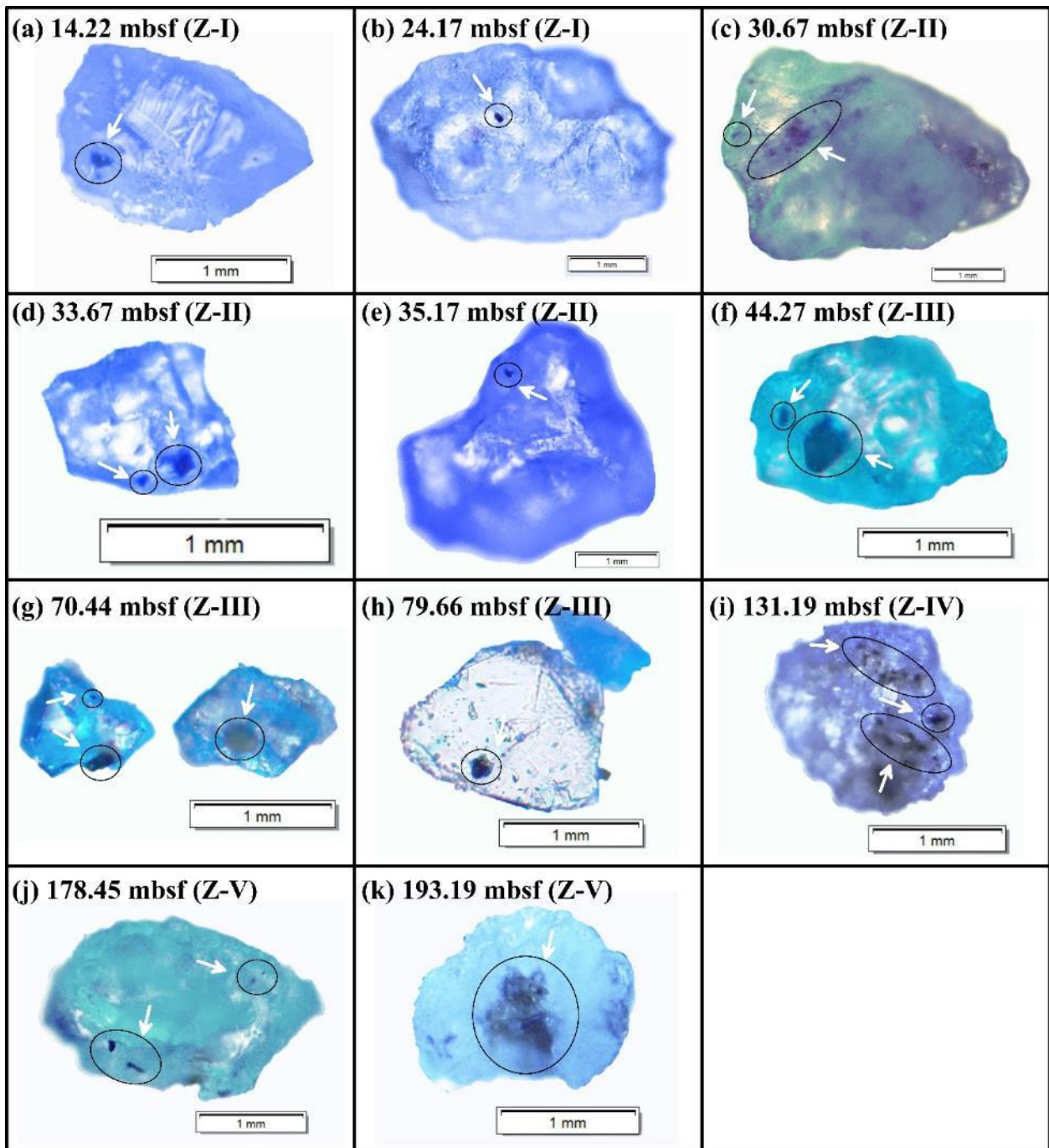


**Fig. S4:** (a–k) Optical microscopic images of the representative (>63  $\mu\text{m}$ ) fraction from deep-seated (Core ID: NGHP-01-15A) gas hydrate site in the Krishna-Godavari (K-G), Bay of Bengal. Magnetic inclusion within host quartz (>63  $\mu\text{m}$ ) fractions are marked (see black circles and white arrows).

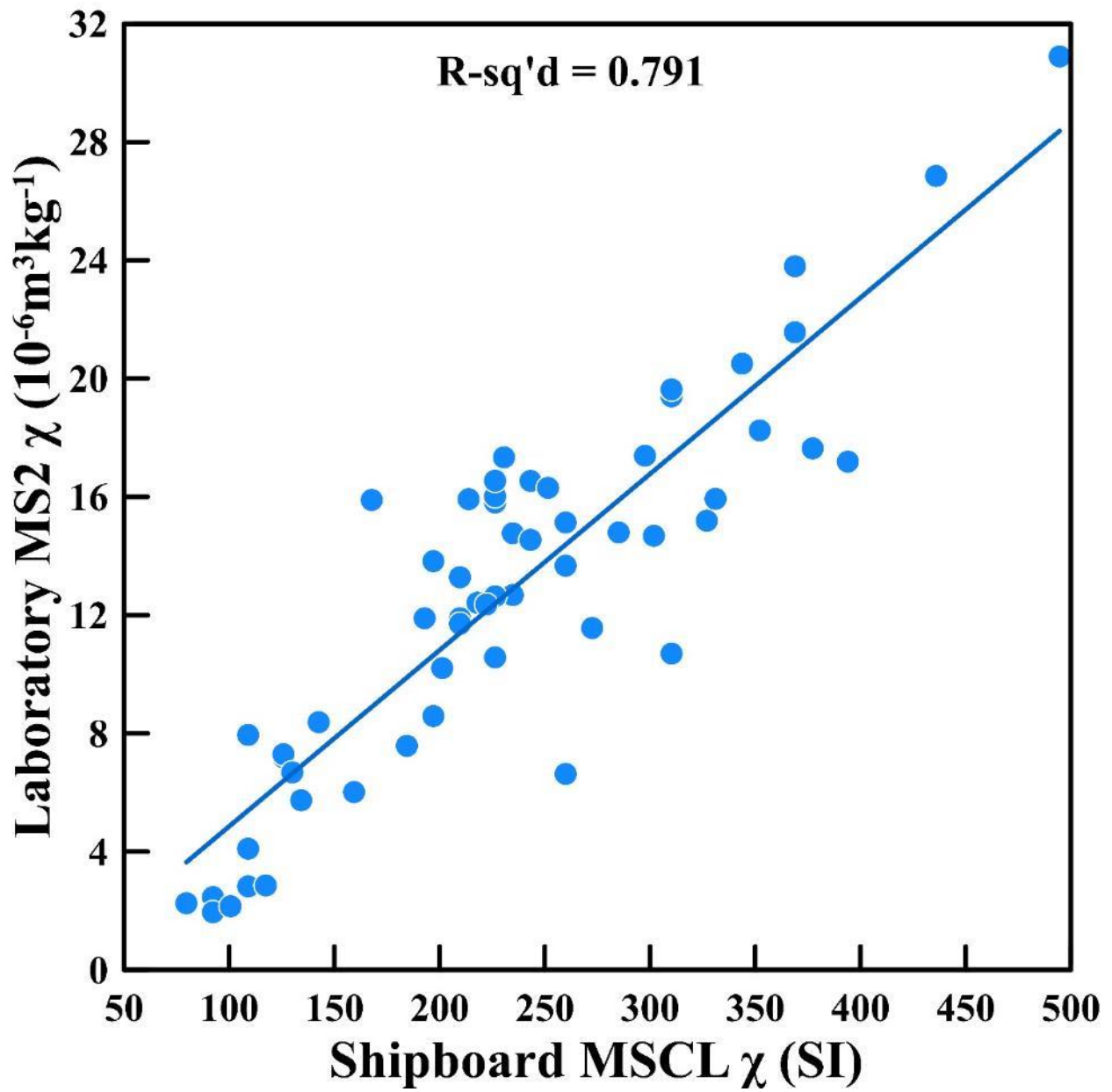


**Fig. S5:** Bivariate plot of volume-specific shipboard MSCL magnetic susceptibility (2006) and laboratory-based mass-normalized magnetic susceptibility ( $\chi$ ) of core NGHP-01-15A.

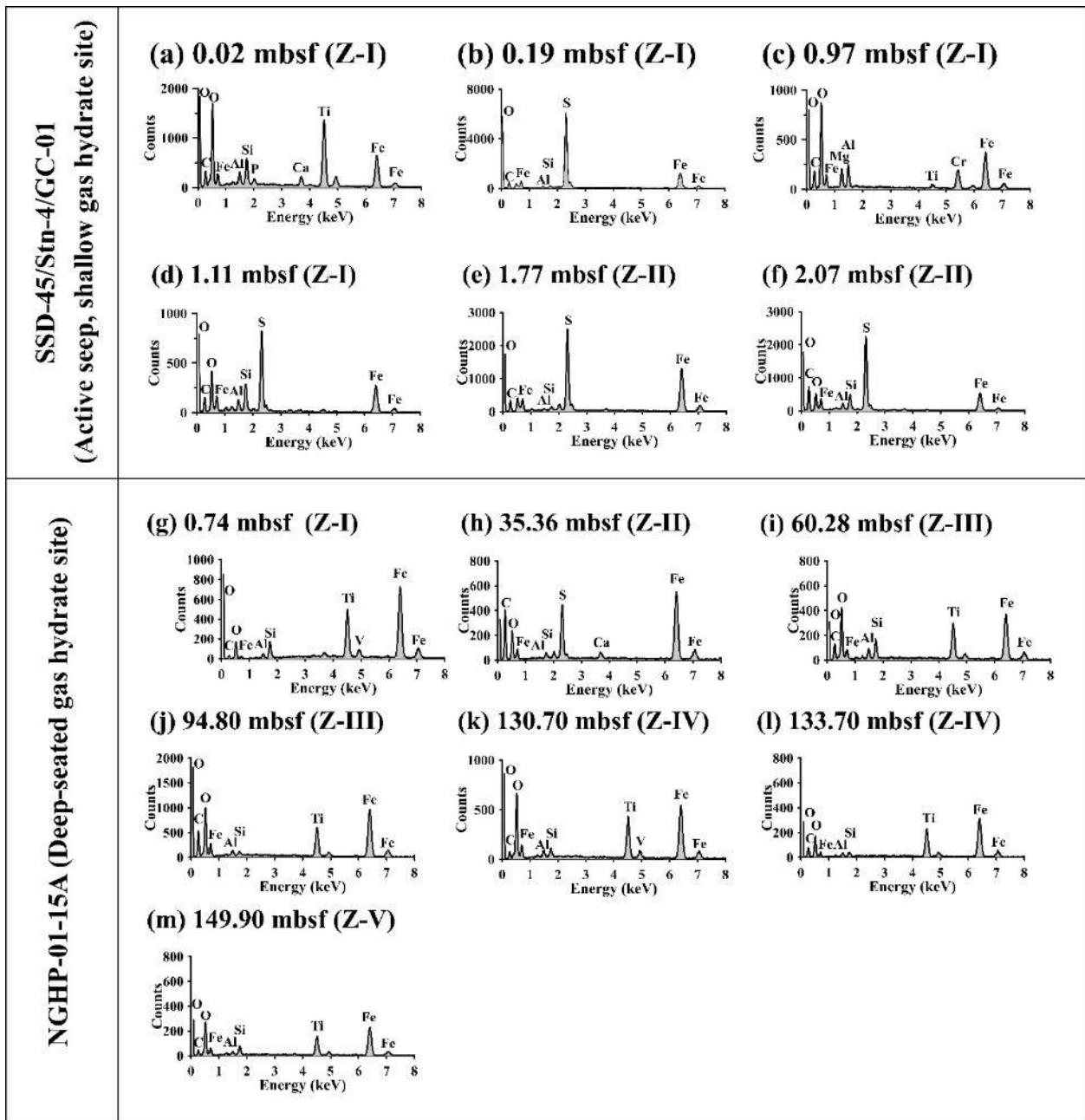


**Fig. S6:** (a-f) Energy dispersive spectroscopy (EDS) data of respective scanning electron microscopy (SEM) images of the sediment core SSD-45/Stn-4/GC-01 (active seep, shallow gas hydrate site), and (g-m) NGHP-01-15A (deep-seated gas hydrate site) presented in Fig. 6.



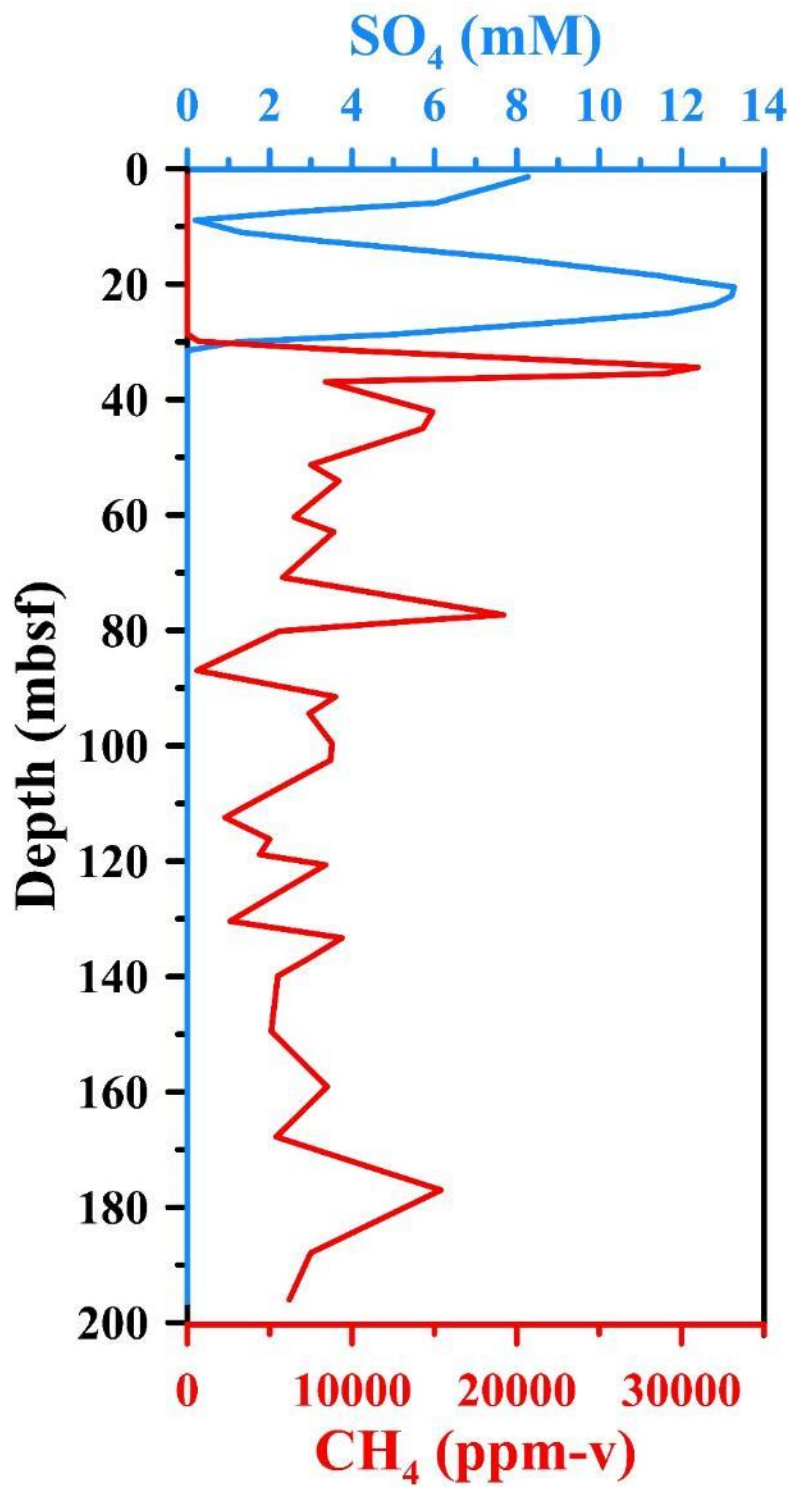


**Fig. S7:** Pore-water sulfate concentration and methane (headspace gas) profile of sediment core NGHP-01-15A (modified from *Collet et al., 2008*).

**Table- 1:** Depth-wise distribution of authigenic carbonates in a sediment core from shallow (active cold seep; Core ID: SSD-45/Stn-4/GC-01) gas hydrate site in the Krishna-Godavari (K-G) basin, Bay of Bengal.

Depth (mbsf)	No. of Carbonate Pieces	Carbonate Size	Depth (mbsf)	No. of Carbonate Pieces	Carbonate Size
0.01	4-5 Pieces	Small + Medium Pieces	0.73	3 Pieces	Medium to Large
0.03	4-5 Pieces	Small Pieces	0.75	4 Pieces	Medium to Large
0.05	3-4 Pieces	Small Pieces	0.77	6 Pieces	Medium to Large
0.07	3-4 Pieces	Small Pieces	0.79	4 Pieces	Medium to Large
0.09	3-4 Pieces	Small+ Medium Pieces	0.81	5 Pieces	Medium to Large
0.11	4 Pieces	Small Pieces	0.83	3 Pieces	Medium to Large
0.13	4 Pieces	Small Pieces	0.85	2 Pieces	Medium to Large
0.15	3 Pieces	Small Pieces	0.87	2 Pieces	Medium to Large
0.17	3 Pieces	Small Pieces	0.89	3 Pieces	Medium to Large
0.18	4 Pieces	Medium to Large	0.91	3 Pieces	Medium to Large
0.21	3 Pieces	Medium to Large	0.93	4 Pieces	Medium to Large
0.23	2 Pieces	Medium to Large	0.95	3 Pieces	Medium to Large
0.25	4 Pieces	Medium to Large	0.97	3 Pieces	Medium to Large
0.27	3 Pieces	Medium to Large	0.99	3 Pieces	Medium to Large
0.29	5 Pieces	Medium to Large	1.01	More than 10 Pieces	Medium to Large
0.31	3 Pieces	Medium to Large	1.03	4 Pieces	Medium to Large
0.33	4 Pieces	Medium to Large	1.05	--	--
0.35	5 Pieces	Medium to Large	1.07	3 Pieces	Medium to Large
0.37	5 Pieces	Medium to Large	1.09	3 Pieces	Medium to Large
0.39	5 Pieces	Medium to Large	1.11	4 Pieces	Medium to Large
0.41	3 Pieces	Medium to Large	1.13	2 Pieces	Medium to Large
0.43	5 Pieces	Medium to Large	1.14	2 Pieces	Medium to Large
0.45	4 Pieces	Medium to Large	1.17	2 Pieces	Small Pieces
0.46	6 Pieces	Medium to Large	1.19	1 Piece	Small to Medium
0.49	4 Pieces	Medium to Large	1.21	1 Piece	Small to Medium
0.51	3 Pieces	Medium to Large	1.23	1 Piece	Small to Medium
0.53	4 Pieces	Medium to Large	1.25	3 Pieces	Small to Medium
0.55	2 Pieces	Medium to Large	1.27	2 Pieces	Small to Medium
0.57	2 Pieces	Medium to Large	1.29	3 Pieces	Small to Medium
0.59	3 Pieces	Medium to Large	1.31	1 Piece	Small to Medium
0.61	3 Pieces	Medium to Large	1.33	2 Pieces	Small to Medium
0.63	3 Pieces	Medium to Large	1.35	--	--
0.65	1 Piece	Large	1.37	3 Pieces	Small to Medium
0.67	2 Pieces	Medium to Large	1.39	1 Piece	Small to Medium
0.69	2 Pieces	Medium to Large	1.41	--	--
0.71	4 Pieces	Medium to Large	1.43	1 Piece	Small to Medium
1.45	1 Piece	Small to Medium			
1.47	1 Piece	Small to Medium			
1.49	1 Piece	Small to Medium			

---

1.51	--	--
1.53	1 Piece	Small to Medium
1.55	-	-
1.57	4 Pieces	Small to Medium
1.59	--	--
1.61	--	--
1.63	--	--
1.65	--	--
1.67	--	--
1.69	--	--
1.71	--	--
1.73	--	--
1.75	--	--
1.77	--	--
1.79	--	--
1.81	--	--
1.83	--	--
1.85	--	--
1.87	--	--
1.89	--	--
1.91	--	--
1.93	--	--
1.95	--	--
1.97	--	--
1.99	--	--
2.01	--	--
2.03	--	--
2.05	--	--
2.07	--	--
2.09	--	--
2.11	--	--
2.13	--	--
2.15	--	--
2.17	--	--
2.19	--	--
2.21	--	--
2.23	--	--

---

**Table-2:** Depth-wise distribution of authigenic carbonates in a sediment core from deep-seated (Core ID: NGHP-01-15A) gas hydrate site in the Krishna-Godavari (K-G) basin, Bay of Bengal (modified after *Teichert et al. 2014*).

<b>Depth(mbsf)</b>	<b>Lithology</b>	<b>Carbonate composition</b>
47.2	Nodule	Fe-rich-carbonate
47.8	Nodule	Fe-rich-carbonate
55.9	Nodule	Fe-rich-carbonate
58.4	Nodule	Fe-rich-carbonate
60.2	Nodule	Fe-rich-carbonate
62	Nodule	Fe-rich-carbonate
63.9	Nodule	Fe-rich-carbonate
64.1	Nodule	Fe-rich-carbonate
72.9	Nodule	Fe-rich-carbonate
73	Nodule	Fe-rich-carbonate
73.1	Nodule	Fe-rich-carbonate
87.2	Nodule	Fe-rich-carbonate
108.5	Nodule	Fe-rich-carbonate
111.1	Nodule	LMC
113.6	Nodule	LMC
116.6	Nodule	Fe-rich-carbonate
117.4	Nodule	Fe-rich-carbonate
119.3	Nodule	Fe-rich-carbonate
128.5	Nodule	Fe-rich-carbonate
128.6	Nodule	Fe-rich-carbonate
129.4	Nodule	Fe-rich-carbonate
130.3	Nodule	Fe-rich-carbonate
146.8	Nodule	Ca-rich dolomite/ankerite
157.3	Nodule	HMC
157.3	Nodule	Fe-rich-carbonate
158.3	Nodule	LMC
163.7	Nodule	LMC
167.4	Nodule	Fe-rich-carbonate
167.7	Nodule	Fe-rich-carbonate
179	Nodule	low calcium-carbonate
195.3	Nodule	Fe-rich-carbonate

**Table-3** Depth-wise distribution of sand layers in sediment core from deep-seated (Core ID: NGHP-01-15A) gas hydrate site in the Krishna-Godavari (K-G) basin, Bay of Bengal (modified after *Collett et al., 2008*).

Depth (mbsf)	Type of occurrence	Depth (mbsf)	Type of occurrence	Depth (mbsf)	Type of occurrence
15.83	sand bed	31.42	sand bed	92.61	sand laminae
15.84	sand bed	35.34	sand bed	92.7	sand laminae
25.95	sand bed	35.54	sand bed	92.83	sand laminae
25.98	sand bed	36.27	sand bed	92.86	sand laminae
27.27	sand bed	36.46	sand bed	90.4	sand pocket
27.3	sand bed	36.485	sand bed	90.45	sand pocket
27.81	sand bed	36.555	sand bed	100.33	sand bed
28.44	sand bed	36.805	sand bed	100.4	sand bed
35.31	sand bed	36.82	sand bed	110.63	sand burrow fill
31.63	sand bed	39.28	sand bed	109.08	sand laminae
34.42	sand bed	38.13	sand bed	132.47	multiple silt/sand laminae
31.29	sand bed	39.08	sand bed	132.17	multiple silt/sand laminae
36.32	sand bed	56.21	sand bed	131.43	multiple silt/sand laminae
36.4	sand bed	56.25	sand bed	130.47	sand bed
30.75	sand bed	56.3	sand bed	178.12	sand bed
30.97	sand bed	56.35	sand bed	179.42	sand bed
31.2	sand bed	67.61	sand bed	181.7	sand bed
31.23	sand bed	67.5	sand bed	178.18	sand bed
34.73	sand bed	70.57	sand bed	178.23	sand bed
36.35	sand bed	70.67	sand bed	178.315	sand bed
29.09	sand bed	70.84	sand bed	179.11	sand bed
29.23	sand bed	71.56	sand bed	183.36	sand bed
29.27	sand bed	72.09	sand bed	186.83	sand bed
29.8	sand bed	73.01	sand bed	191.95	sand bed
29.9	sand bed	77.4	sand bed	191.99	sand bed
30.14	sand bed	78.17	multiple Sand bed	192.12	sand bed
30.16	sand bed	77.24	multiple Sand bed	192.17	sand bed
30.19	sand bed	76.9	multiple Sand bed	192.23	sand bed
30.21	sand bed	79.63	multiple Sand bed	192.28	sand bed
30.23	sand bed	79.88	multiple Sand bed	192.45	sand bed
30.28	sand bed	77.37	multiple Sand bed	192.48	sand bed
30.65	sand bed	76.15	multiple Sand bed		
30.67	sand bed	79.98	multiple Sand bed		
30.71	sand bed	80.06	multiple Sand bed		
30.91	sand bed	78.23	sand bed		
31.16	sand bed	78.3	sand bed		

## Data availability statement

The data used in this study is available on CSIR-NIO repository. The link to access data online is <https://publication-data.nio.org/s/mGsfeYt2RN3eQo5>

## References

Aloisi, G., Pierre, C., Rouchy, J.M., Foucher, J.P., Woodside, J., 2000. Methane-related authigenic carbonates of eastern Mediterranean Sea mud volcanoes and their possible relation to gas hydrate destabilization. *Earth Planet. Sci. Lett.* 184(1), pp.321-338. [https://doi.org/10.1016/S0012-821X\(00\)00322-8](https://doi.org/10.1016/S0012-821X(00)00322-8)

Aloisi, G., Wallmann, K., Drews, M. and Bohrmann, G., 2004. Evidence for the submarine weathering of silicate minerals in Black Sea sediments: possible implications for the marine Li and B cycles. *Geochemistry, Geophysics, Geosystems*, 5(4). <http://dx.doi.org/10.1029/2003GC000639>.

Amiel, N., Shaar, R., Sivan, O., 2020. The Effect of Early Diagenesis in Methanic Sediments on Sedimentary Magnetic Properties: Case Study From the SE Mediterranean Continental Shelf. *Front. Earth Sci.* 8:283. <https://doi.org/10.3389/feart.2020.00283>

Badesab, F., Dewangan, P., Gaikwad, V., Kars, M., Kocherla, M., Krishna, K.S., et al., 2019. Magnetic mineralogical approach for exploration of gas hydrates in the Bay of Bengal. *J. Geophys. Res. Solid Earth.* 24(5), 4428–4451. <https://doi.org/10.1029/2019JB017466>

Badesab, F., Gaikwad, V., Dewangan, P., 2020a. Controls on greigite preservation in a gas hydrate system of the Krishna-Godavari basin, Bay of Bengal. *Geo-Mar. Lett.* 40(4), 439-452. <https://doi.org/10.1007/s00367-019-00604-z>

Badesab, F., Dewangan, P., Gaikwad, V., Sebastian, J. G., Venkateshwarlu, M., 2020b. A rock magnetic perspective of gas hydrate occurrences in a high-energy depositional system in the Krishna-Godavari basin, Bay of Bengal. *Geo-Mar. Lett.* 1-15. <https://doi.org/10.1007/s00367-020-00646-8>

Badesab, F., Dewangan, P., Gaikwad, V., 2020c. Magnetic mineral diagenesis in a newly discovered active cold seep site in the Bay of Bengal. *Front. Earth Sci.* <https://doi.org/10.3389/feart.2020.592557>

Badesab, F., Dewangan, P., Usapkar, A., Kocherla, M., Peketi, A., Mohite, K., et al., 2017. Controls on evolution of gas-hydrate system in the Krishna-Godavari basin, offshore India. *Geochem., Geophys., Geosys.* 18(1), 52–74. <https://doi.org/10.1002/2016GC006606>

Badesab, F., Gaikwad, V., Venkateshwarlu, M., Kadam, N. and João, H.M., 2022. Diagenetic dissolution, maghemitization and sulphidization of magnetic minerals in rapidly deposited gas hydrate bearing sediments from the Bay of Bengal. *Marine and Petroleum Geology*, p.105585. <https://doi.org/10.1016/j.marpetgeo.2022.105585>

Bastia, R., 2007. Geologic settings and petroleum systems of India's east coast offshore basins: Concepts and applications. Bangalore, India: Technology Publications.

Besnus, M. J., Meyer, A. J., 1964. Nouvelles données expérimentales sur le magnétisme de la pyrrhotine naturelle. In *Proc. Int. Conf. Mag.* (Vol. 20, pp. 507-511).

Blanchet, C. L., Thouveny, N., Vidal, L., 2009. Formation and preservation of greigite (Fe<sub>3</sub>S<sub>4</sub>) in sediments from the Santa Barbara Basin: Implications for paleoenvironmental changes during the past 35 ka. *Paleoceanography* 24(2). <https://doi.org/10.1029/2008PA001719>

Bloemendal, J., King, J.W., Hall, F.R., Doh, S.J., 1992. Rock magnetism of late Neogene and Pleistocene deep-sea sediments: relationship to sediment source, diagenetic processes, and sediment lithology. *J. Geophys. Res. Solid Earth*, 96:4361–4375 <https://doi.org/10.1029/91JB03068>

Canfield, D. E., Berner, R. A., 1987. Dissolution and pyritization of magnetite in anoxic marine sediments. *Geochim. Cosmochim. Acta.* 51(3), 645–659. [https://doi.org/10.1016/0016-7037\(87\)90076-7](https://doi.org/10.1016/0016-7037(87)90076-7)

Chang, L., Roberts, A.P., Heslop, D., Hayashida, A., Li, J., Zhao, X. et al., 2016. Widespread occurrence of silicate-hosted magnetic mineral inclusions in marine sediments and their contribution to paleomagnetic recording. *J. Geophys. Res. Solid Earth.* 121(12):8415–8431. <https://doi.org/10.1002/2016JB013109>

Collett, T., Riedel, M., Cochran, J. R., Boswell, R., Presley, J., Kumar, P., et al., and the NGHP Expedition 01 Scientists, 2008. Indian National Gas Hydrate Program, Expedition - 01, Initial report, Directorate General of Hydrocarbons, Ministry of Petroleum and Natural gas, India.

Collett, T.S., Kumar, P., Boswell, R. and Waite, W., 2019. Preface: Marine gas hydrate reservoir systems along the eastern continental margin of India: Results of the National Gas Hydrate Program Expedition 02. *Journal of Marine and Petroleum Geology*, 108, pp.1-2. <https://doi.org/10.1016/j.marpetgeo.2019.03.005>

Collett, T. S., Boswell, R., Cochran, J. R., Kumar, P., Lall, M., Mazumdar, A., et al., 2014. Geologic implications of gas hydrates in the offshore of India: Results of the National Gas Hydrate Program Expedition 01. *Mar. Pet. Geol.* 58, 3–28. <https://doi.org/10.1016/j.marpetgeo.2014.07.021>

Day R., Fuller M., Schmidt V.A., 1977. Hysteresis properties of titanomagnetites: grain-size and compositional dependence. *Phys. Earth. Planet. Inter.* 13(4):260–267. [https://doi.org/10.1016/0031-9201\(77\)90108-X](https://doi.org/10.1016/0031-9201(77)90108-X)

Dekkers, M. J., 1989. Magnetic properties of natural pyrrhotite. II. High- and low-temperature behaviour of J<sub>r</sub>s and TRM as function of grain size. *Phys. Earth Planet. Inter.* 57, 266–283. [https://doi.org/10.1016/0031-9201\(89\)90116-7](https://doi.org/10.1016/0031-9201(89)90116-7)

Dewangan, P., Sriram, G., Kumar, A., Mazumdar, A., Peketi, A., Mahale, V. et al., 2021. Widespread occurrence of methane seeps in deep-water regions of Krishna-Godavari basin, Bay of Bengal. *Mar. Pet. Geol.* 124 104783. <https://doi.org/10.1016/j.marpetgeo.2020.104783>

Dewangan, P., Basavaiah, N., Badesab, F. K., Usapkar, A., Mazumdar, A., Joshi, R., et al., 2013. Diagenesis of magnetic minerals in a gas hydrate/cold seep environment off the Krishna–Godavari basin, Bay of Bengal. *Mar. Geol.* 340, 57–70. <https://doi.org/10.1016/j.marpetgeo.2013.04.016>

Dewangan, P., Ramprasad, T., Ramana, M. V., Mazumdar, A., Desa, M., Badesab, F. K., 2010. Seabed morphology and gas venting features in the continental slope region of Krishna-Godavari basin, Bay of Bengal: Implications in gas-hydrate exploration. *Mar. Petrol. Geol.* 27(7), 1628–1641. <https://doi.org/10.1016/j.marpetgeo.2010.03.015>

- Dewangan, P., Sriram, G., Ramprasad, T., Ramana, M. V., Jaiswal, P., 2011. Fault system and thermal regime in the vicinity of site NGHP-01-10, Krishna–Godavari basin, Bay of Bengal. *Mar. Petrol. Geol.* 28, 1899–1914. <https://doi.org/10.1016/j.marpetgeo.2011.03.009>
- Dillon, M., Bleil, U., 2006. Rock magnetic signatures in diagenetically altered sediments from the Niger deep-sea fan. *J. Geophys. Res. Solid Earth.* 111(B3). <https://doi.org/10.1029/2004JB003540>
- Dunlop, D. J., Özdemir, Ö., Schmidt, P. W., 1997. Paleomagnetism and paleothermometry of the Sydney Basin 2. Origin of anomalously high unblocking temperatures. *J. Geophys. Res.* 102(B12), 27, 285–295. <https://doi.org/10.1029/97JB02478>
- Egger, M., Rasigraf, O., Sapart, C.J., Jilbert, T., Jetten, M.S., Röckmann, T., Van der Veen, C., Banda, N., Kartal, B., Ettwig, K.F., Slomp, C.P., 2015. Iron-mediated anaerobic oxidation of methane in brackish coastal sediments. *Environ. Sci. Technol.* 49(1), pp.277-283. <https://doi.org/10.1021/es503663z>
- Enkin, R. J., Baker, J., Nourgaliev, D., Iassonov, P., Hamilton, T. S., 2007. Magnetic hysteresis parameters and Day plot analysis to characterize diagenetic alteration in gas hydrate-bearing sediments. *J. Geophys. Res. Solid Earth.* 112, B06S90. <https://doi.org/10.1029/2006JB004638>
- Esteban, L., Enkin, R. J., Hamilton, T., 2008. Gas hydrates and magnetism: Comparative geological settings for diagenetic analysis. *Proceedings of the 6th International Conference on Gas Hydrates* (pp. 1-9).
- Gaikwad, V. V., Badesab, F. K., Dewangan, P., Kotha, M., 2021. Diagenesis of Magnetic Minerals in Active/Relict Methane Seep: Constraints from Rock Magnetism and Mineralogical Records from Bay of Bengal. *Front. Earth Sci.* 9, 60. <https://doi.org/10.3389/feart.2021.638594>
- Garming, J. F. L., Bleil, U., Riedinger, N., 2005. Alteration of magnetic mineralogy at the sulfate–methane transition: Analysis of sediments from the Argentine continental slope. *Phys. Earth Planet. Inter.* 151(3-4), 290–308. <https://doi.org/10.1016/j.pepi.2005.04.001>
- Greve, A., Kars, M., Dekkers, M. J., 2021. Fluid accumulation, migration and anaerobic oxidation of methane along a major splay fault at the Hikurangi subduction margin (New Zealand): A magnetic approach. *J. Geophys. Res. Solid Earth.* 126(2), e2020JB020671. <https://doi.org/10.1029/2020JB020671>
- Halgedahl, S. L., Jarrard, R. D., 1995. Low-temperature behavior of single-domain through multidomain magnetite. *Earth Planet. Sci. Lett.* 130(1-4), 127-139. [https://doi.org/10.1016/0012-821X\(94\)00260-6](https://doi.org/10.1016/0012-821X(94)00260-6)
- Harrison, R. J., Feinberg, J. M. 2008. FORCinel: An improved algorithm for calculating first order reversal curve distributions using locally weighted regression smoothing. *Geochem., Geophys., Geosys.* 9, Q05016. <https://doi.org/10.1029/2008GC001987>
- Hatfield, R. G., 2014. Particle size-specific magnetic measurements as a tool for enhancing our understanding of the bulk magnetic properties of sediments. *Minerals* 4(4), 758-787. <https://doi.org/10.3390/min4040758>
- Hirt, A. M., Gehring, A. U., 1991. Thermal alteration of the magnetic mineralogy in ferruginous rocks. *J. Geophys. Res. Solid Earth.* 96(B6), 9947–9953. <https://doi.org/10.1029/91JB00573>



- Hirt, A. M., Lowrie, W., Clendenen, W. S., Kligfield, R., 1993. Correlation of strain and the anisotropy of magnetic susceptibility in the Onaping Formation: evidence for a near-circular origin of the Sudbury basin. *Tectonophysics* 225(4), 231–254. [https://doi.org/10.1016/0040-1951\(93\)90300-9](https://doi.org/10.1016/0040-1951(93)90300-9)
- Horng, C. S., 2018. Unusual magnetic properties of sedimentary pyrrhotite in methane seepage sediments: Comparison with metamorphic pyrrhotite and sedimentary greigite. *J. Geophys. Res. Solid Earth*. 123(6), 4601-4617. <https://doi.org/10.1002/2017JB015262>
- Hounslow, M. W., Maher, B. A., 1996. Quantitative extraction and analysis of carriers of magnetization in sediments. *Geophys. J. Int.* 124(1), 57-74. <https://doi.org/10.1111/j.1365-246X.1996.tb06352.x>
- Itambi, A. C., Von Dobeneck, T., Dekkers, M. J., Frederichs, T., 2010. Magnetic mineral inventory of equatorial Atlantic Ocean marine sediments off Senegal—glacial and interglacial contrast. *Geophys. J. Int.* 183(1), 163-177. <https://doi.org/10.1111/j.1365-246X.2010.04736.x>
- Jiang, W. T., Horng, C. S., Roberts, A. P., Peacor, D. R., 2001. Contradictory magnetic polarities in sediments and variable timing of neof ormation of authigenic greigite. *Earth Planet. Sci. Lett.* 193(1-2), 1-12. [https://doi.org/10.1016/S0012-821X\(01\)00497-6](https://doi.org/10.1016/S0012-821X(01)00497-6)
- João, H. M., Badesab, F., Gaikwad, V., Kocherla, M., Deenadayalan, K., 2021. Controls of mass transport deposit and magnetic mineral diagenesis on the sediment magnetic record from the Bay of Bengal. *Mar. Petrol. Geol.* 128, 104994. <https://doi.org/10.1016/j.marpetgeo.2021.104994>
- Johnson, J.E., Phillips, S.C., Clyde, W.C., Giosan, L., Torres, M.E., 2021. Isolating detrital and diagenetic signals in magnetic susceptibility records from methane-bearing marine sediments. *G-cubed* 22 (9), e2021GC009867. <https://doi.org/10.1029/2021GC009867>.
- Johnson, J.E., Phillips, S.C., Torres, M.E., Piñero, E., Rose, K.K., Giosan, L., 2014. Influence of total organic carbon deposition on the inventory of gas hydrate in the Indian continental margins. *Mar. Petrol. Geol.* 58, 406–424. <https://doi.org/10.1016/j.marpetgeo.2014.08.021>.
- Kakol, Z., Sabol, J., Stickler, J., Honig, J. M., 1992. Effect of low-level titanium (IV) doping on the resistivity of magnetite near the Verwey transition. *Phys. Rev. B* 46(4), 1975. <https://doi.org/10.1103/PhysRevB.46.1975>
- Kao, S. J., Horng, C. S., Roberts, A. P., Liu, K. K., 2004. Carbon–sulfur–iron relationships in sedimentary rocks from southwestern Taiwan: influence of geochemical environment on greigite and pyrrhotite formation. *Chem. Geol.* 203(1-2), 153-168. <https://doi.org/10.1016/j.chemgeo.2003.09.007>
- Karlin, R., Lyle, M., Heath, G. R., 1987. Authigenic magnetite formation in suboxic marine sediments. *Nature* 326(6112), 490-493.
- Kars, M., Kodama, K., 2015. Authigenesis of magnetic minerals in gas hydrate bearing sediments in the Nankai Trough, Offshore Japan. *Geochem., Geophys., Geosys.* 16, 947–961. <https://doi.org/10.1002/2014GC005614>
- Kars, M., Musgrave, R. J., Hoshino, T., Jonas, A. S., Bauersachs, T., Inagaki, F., Kodama, K., 2018. Magnetic mineral diagenesis in a high temperature and deep methanic zone in Izu rear arc marine sediments, northwest Pacific Ocean. *J. Geophys. Res. Solid Earth*. 123(10), 8331-8348. <https://doi.org/10.1029/2018JB015861>

- Kars, M., Greve, A., Zerbst, L., 2021. Authigenic greigite as an indicator of methane diffusion in gas hydrate-bearing sediments of the Hikurangi Margin, New Zealand. *Front. Earth Sci.* 9, 80. <https://doi.org/10.3389/feart.2021.603363>
- Karstens, J., Haflidason, H., Becker, L. W., Berndt, C., Rüpke, L., Planke, S., et al., 2018. Glacigenic sedimentation pulses triggered postglacial gas hydrate dissociation. *Nat. Commun.* 9(1), 635. <https://doi.org/10.1038/s41467-018-03043-z>
- Kasten, S., Jørgensen, B. B., 2000. Sulfate reduction in marine sediments. In *Marine geochemistry* (pp. 263-281). Springer, Berlin, Heidelberg.
- Krishna, K. S., Ismaiel, M., Srinivas, K., Gopala Rao, D., Mishra, J., Saha, D., 2016. Sediment pathways and emergence of Himalayan source material in the Bay of Bengal. *Curr. Sci.* 110. <https://doi.org/10.18520/cs/v110/i3/363-372>
- Kumar, P., Collett, T. S., Boswell, R., Cochran, J. R., Lall, M., Mazumdar, A., et al., 2014. Geologic implications of gas hydrates in the offshore of India: Krishna-Godavari Basin, Mahanadi Basin, Andaman Sea, Kerala-Konkan Basin. *Mar. Petrol. Geol.* 58, 29–98. <https://doi.org/10.1016/j.marpetgeo.2014.07.031>
- Kvenvolden, K.A., 1993. Gas hydrates—geological perspective and global change. *Reviews of geophysics*, 31(2), pp.173-187. <https://doi.org/10.1029/93RG00268>
- Larrasoña, J. C., Roberts, A. P., Musgrave, R. J., Gràcia, E., Piñero, E., Vega, M., et al., 2007. Diagenetic formation of greigite and pyrrhotite in gas hydrate marine sedimentary systems. *Earth Planet. Sci. Lett.* 261(3-4), 350–366. <https://doi.org/10.1016/j.epsl.2007.06.032>
- Larrasoña, J. C., Roberts, A. P., Stoner, J. S., Richter, C., Wehausen, R., 2003. A new proxy for bottom-water ventilation in the eastern Mediterranean based on diagenetically controlled magnetic properties of sapropel-bearing sediments. *Palaeogeogr., Palaeoclimatol., Palaeoecol.* 190, 221-242. [https://doi.org/10.1016/S0031-0182\(02\)00607-7](https://doi.org/10.1016/S0031-0182(02)00607-7)
- Lascu, I., Einsle, J. F., Ball, M. R., Harrison, R. J., 2018. The vortex state in geologic materials: A micromagnetic perspective. *J. Geophys. Res. Solid Earth.* 123, 7285–7304. <https://doi.org/10.1029/2018JB015909>
- Lattard, D., Engelmann, R., Kontny, A., Sauerzapf, U., 2006. Curie temperatures of synthetic titanomagnetites in the Fe-Ti-O system: Effects of composition, crystal chemistry, and thermomagnetic methods. *J. Geophys. Res. Solid Earth.* 111(B12). <https://doi.org/10.1029/2006JB004591>
- Liang, Q., Hu, Y., Feng, D., Peckmann, J., Chen, L., Yang, S., Liang, J., Tao, J., Chen, D., 2017. Authigenic carbonates from newly discovered active cold seeps on the northwestern slope of the South China Sea: Constraints on fluid sources, formation environments, and seepage dynamics. *Deep Sea Res. Part I Oceanogr. Res. Pap.* 124, pp.31-41. <https://doi.org/10.1016/j.dsr.2017.04.015>
- Lin, Z., Sun, X., Roberts, A.P., Strauss, H., Lu, Y., Yang, X., et al., 2020. A novel authigenic magnetite source for sedimentary magnetization. *Geology*. 49(4), 360-365. <https://doi.org/10.1130/G48069.1>
- Liu, Q., Roberts, A. P., Larrasoña, J. C., Banerjee, S. K., Guyodo, Y., Tauxe, L., et al., 2012. Environmental magnetism: principles and applications. *Rev. Geophys.* 50:RG4002. <https://doi.org/10.1029/2012RG000393>

- Lougheed, B. C., Snowball, I., Moros, M., Kabel, K., Muscheler, R., Virtasalo, J. J., Wacker, L., 2012. Using an independent geochronology based on palaeomagnetic secular variation (PSV) and atmospheric Pb deposition to date Baltic Sea sediments and infer 14C reservoir age. *Quat. Sci. Rev.* 42, 43-58. <https://doi.org/10.1016/j.quascirev.2012.03.013>
- Lovley, D. R., Stolz, J. F., Nord, G. L., Phillips, E. J., 1987. Anaerobic production of magnetite by a dissimilatory iron-reducing microorganism. *Nature* 330(6145), 252-254. <https://doi.org/10.1038/330252a0>
- Luff, R., Greinert, J., Wallmann, K., Klauke, I., Suess, E., 2005. Simulation of long-term feedbacks from authigenic carbonate crust formation at cold vent sites. *Chem. Geol.* 216(1-2), 157-174. <https://doi.org/10.1016/j.chemgeo.2004.11.002>
- Maher, B. A., Thompson, R., 1999. Quaternary climates, environments and magnetism. Cambridge University Press.
- Mazumdar, A., Dewangan, P., João, H.M., Peketi, A., Khosla, V.R., Kocherla, M., et al., 2009. Evidence of paleo-cold seep activity from the Bay of Bengal, offshore India. *Geochem., Geophys., Geosys.*, 10Q06005. <https://doi.org/10.1029/2008GC002337>
- Mazumdar A., Dewangan P., Peketi A., Gullapalli S., Kalpana M. S., Naik G. P., et al., 2019. The first record of active methane (cold) seep ecosystem associated with shallow methane hydrate from the Indian EEZ. *J. Earth Sys. Sci.* 128:18, <https://doi.org/10.1007/s12040-018-1044-y>
- Moskowitz, B. M., Jackson, M., Kissel, C., 1998. Low-temperature magnetic behavior of titanomagnetites. *Earth Planet. Sci. Lett.* 157(3-4), 141-149. [https://doi.org/10.1016/S0012-821X\(98\)00033-8](https://doi.org/10.1016/S0012-821X(98)00033-8)
- Musgrave, R. J., Bangs, N. L., Larrasoña, J. C., Gràcia, E., Hollamby, J. A., Vega, M. E., 2006. Rise of the base of the gas hydrate zone since the last glacial recorded by rock magnetism. *Geology* 34(2), 117-120. <https://doi.org/10.1130/G22008.1>
- Musgrave, R. J., Kars, M., Vega, M. E., 2019. Progressive and punctuated magnetic mineral diagenesis: The rock magnetic record of multiple fluid inputs and progressive pyritization in a volcano-bounded basin, IODP Site U1437, Izu rear arc. *J. Geophys. Res. Solid Earth.* 124(6), 5357-5378. <https://doi.org/10.1029/2018JB017277>
- Muxworthy, A. R., Dunlop, D. J., 2002. First-order reversal curve (FORC) diagrams for pseudo-single-domain magnetites at high temperature. *Earth Planet. Sci. Lett.* 203(1), 369-382. [https://doi.org/10.1016/S0012-821X\(02\)00880-4](https://doi.org/10.1016/S0012-821X(02)00880-4)
- Niewöhner, C., Hensen, C., Kasten, S., Zabel, M., Schulz, H. D., 1998. Deep sulfate reduction completely mediated by anaerobic methane oxidation in sediments of the upwelling area off Namibia. *Geochim. Cosmochim. Acta.* 62(3), 455-464. [https://doi.org/10.1016/S0016-7037\(98\)00055-6](https://doi.org/10.1016/S0016-7037(98)00055-6)
- Oda, H., Torii, M., 2004. Sea-level change and remagnetization of continental shelf sediments off New Jersey (ODP Leg 174A): magnetite and greigite diagenesis. *Geophys. J. Int.* 156(3), 443-458. <https://doi.org/10.1111/j.1365-246X.2004.02162.x>
- Party, S.S., 1996. Site 997. Proc. ODP Initial Repts.[CD-ROM], 1996, 164, pp.277-334.

- Passier, H. F., Dekkers, M. J., De Lange, G. J., 2000. Rock-magnetic properties, geochemistry and diagenesis of eastern Mediterranean surface sediments. *Geol. Carpath.* 51(3), 189-190.
- Passier, H. D., De Lange, G. J., Dekkers, M. J., 2001. Magnetic properties and geochemistry of the active oxidation front and the youngest sapropel in the eastern Mediterranean Sea. *Geophys. J. Int.* 145(3), 604–614. <https://doi.org/10.1046/j.0956-540x.2001.01394.x>
- Passier, H.F. and Dekkers, M.J., 2002. Iron oxide formation in the active oxidation front above sapropel S1 in the eastern Mediterranean Sea as derived from low-temperature magnetism. *Geophysical Journal International*, 150(1), pp.230-240. <https://doi.org/10.1046/j.1365-246X.2002.01704.x>
- Peters, C., Dekkers, M. J., 2003. Selected room temperature magnetic parameters as a function of mineralogy, concentration and grain size. *Phys. Chem. Earth, Parts A/B/C* 28(16-19), 659-667. [https://doi.org/10.1016/S1474-7065\(03\)00120-7](https://doi.org/10.1016/S1474-7065(03)00120-7)
- Petersen, N., Von Dobeneck T., Vali H., 1986. Fossil bacterial magnetite in deep-sea sediments from the South Atlantic Ocean. *Nature* 320, 611–615. <https://doi.org/10.1038/320611a0>
- Philips, S. C., 2018. Diagenetic degradation of paleoenvironmental signals in magnetic susceptibility in the northern Bay of Bengal, *The IRM Quarterly*, Winter 2017-2018, Vol. 27 No.4
- Phillips, S.C., Johnson, J.E., Underwood, M.B., Guo, J., Giosan, L., Rose, K., 2014. Long timescale variation in bulk and clay mineral composition of Indian continental margin sediments in the Bay of Bengal, Arabian Sea, and Andaman Sea. *Mar. Petrol. Geol.* 58, 117–138. <https://doi.org/10.1016/j.marpetgeo.2014.06.018>.
- Phillips, S. C., Johnson, J. E., Clyde, W. C., Setera, J. B., Maxbauer, D. P., Severmann, S., Riedinger, N., 2017. Rock magnetic and geochemical evidence for authigenic magnetite formation via iron reduction in coal-bearing sediments offshore Shimokita Peninsula, Japan (IODP Site C0020). *Geochem. Geophys. Geosyst.* 18, 2076–2098. <https://doi.org/10.1002/2017GC006943>
- Prabhakar, K.N., Zutshi, P.L., 1993. Evolution of southern part of Indian East Coast basin. *J. Geol. Soc. Ind.* 41:215–230.
- Poulton, S. W., Krom, M. D., Raiswell, R., 2004. A revised scheme for the reactivity of iron (oxyhydr) oxide minerals towards dissolved sulfide. *Geochim. Cosmochim. Acta.* 68(18), 3703-3715. <https://doi.org/10.1016/j.gca.2004.03.012>.
- Ramesh, R., Subramanian, V., 1988, Temporal, spatial and size variation in the sediment transport in the Krishna River basin, India, *J. Hydrol.* 98, 53–65. [https://doi.org/10.1016/0022-1694\(88\)90205-3](https://doi.org/10.1016/0022-1694(88)90205-3)
- Ramprasad, T., Dewangan, P., Ramana, M.V., Mazumdar, A., Karisiddaiah, S.M., Ramya, E.R., et al., 2011. Evidence of slumping/sliding in Krishna–Godavari offshore basin due to gas/fluid movements. *Mar. Petrol. Geol.* 28, 1806–1816. <https://doi.org/10.1016/j.marpetgeo.2011.02.007>
- Rao, G. N., 2001. Sedimentation, stratigraphy, and petroleum potential of Krishna-Godavari basin, East Coast of India. *AAPGB* 85(9), 1623–1643. <https://doi.org/10.1306/8626CCDF-173B-11D7-8645000102C1865D>

- Riedinger, N., Pfeifer, K., Kasten, S., Garming, J. F. L., Vogt, C., Hensen C., 2005. Diagenetic alteration of magnetic signals by anaerobic oxidation of methane related to a change in sedimentation rate, *Geochim. Cosmochim. Acta.* 69, 4117–4126, <https://doi.org/10.1016/j.gca.2005.02.004>.
- Riedinger, N., Formolo, M. J., Lyons, T. W., Henkel, S., Beck, A., Kasten, S., 2014. An inorganic geochemical argument for coupled anaerobic oxidation of methane and iron reduction in marine sediments. *Geobiology* 12(2), 172-181. <https://doi.org/10.1111/gbi.12077>
- Reilly, B. T., McCormick, M. L., Brachfeld, S. A., Haley, B. A., 2020. Authigenic ferrimagnetic iron sulfide preservation due to non-steady state diagenesis: A perspective from Perseverance Drift, North western Weddell Sea. *Geochem., Geophys., Geosys.* e2020GC009380. <https://doi.org/10.1029/2020GC009380>
- Reinholdsson, M., Snowball, I., Zillén, L., Lenz, C., Conley, D.J., 2013. Magnetic enhancement of Baltic Sea sapropels by greigite magnetofossils. *Earth Planet. Sci. Lett.* 366, pp.137-150. <http://dx.doi.org/10.1016/j.epsl.2013.01.029>
- Riedel, M., Collett, T. S., Shankar, U., 2011. Documenting channel features associated with gas hydrates in the Krishna–Godavari Basin, offshore India. *Mar. Geol.* 279(1-4), 1–11. <https://doi.org/10.1016/j.margeo.2010.10.008>
- Riedel, M., Goldberg, D., Guerin, G., 2014. Compressional and shear-wave velocities from gas hydrate bearing sediments: Examples from the India and Cascadia margins as well as Arctic permafrost regions. *Mar. Petrol. Geol.* 58, 292-320. <https://doi.org/10.1016/j.marpetgeo.2014.07.028>
- Roberts, A. P., Zhao, X., Harrison, R. J., Heslop, D., Muxworthy, A. R., Rowan, C. J., et al., 2018. Signatures of reductive magnetic mineral diagenesis from unmixing of first order reversal curves. *J. Geophys. Res. Solid Earth.* 123, 4500–4522. <https://doi.org/10.1029/2018JB015706>
- Roberts, A. P., Chang, L., Rowan, C. J., Horng, C. S., Florindo, F., 2011. Magnetic properties of sedimentary greigite (Fe<sub>3</sub>S<sub>4</sub>): An update. *Rev. Geophys.* 49, RG1002. <https://doi.org/10.1029/2010RG000336>
- Roberts, A. P., Pike, C. R., Verosub, K. L., 2000. First-order reversal curve diagrams: A new tool for characterizing the magnetic properties of natural samples. *J. Geophys. Res. Solid Earth.* 105(B12), 28461-28475. <https://doi.org/10.1029/2000JB900326>
- Roberts, A. P., Almeida, T. P., Church, N. S., Harrison, R. J., Heslop, D., Li, Y., et al., 2017. Resolving the origin of pseudo-single domain magnetic behavior. *J. Geophys. Res. Solid Earth.* 122, 9534–9558. <https://doi.org/10.1002/2017JB014860>
- Roberts, A. P., 2015. Magnetic mineral diagenesis. *Earth-Sci. Rev.* 151, 1–47. <https://doi.org/10.1016/j.earscirev.2015.09.010>
- Rodelli, D., Jovane, L., Giorgioni, M., Rego, E. S., Cornaggia, F., Benites, M., et al., 2019. Diagenetic fate of biogenic soft and hard magnetite in chemically stratified sedimentary environments of Mamanguá Ría, Brazil. *J. Geophys. Res. Solid Earth.* 124 (3), 2313–2330. <https://doi.org/10.1029/2018JB016576>

- Rowan, C. J., Roberts, A. P., 2006. Magnetite dissolution, diachronous greigite formation, and secondary magnetizations from pyrite oxidation: Unravelling complex magnetizations in Neogene marine sediments from New Zealand. *Earth Planet. Sci. Lett.* 241(1-2), 119–137. <https://doi.org/10.1016/j.epsl.2005.10.017>
- Rowan, C. J., Roberts, A. P., 2008. Widespread remagnetizations and a new view of Neogene tectonic rotations within the Australia-Pacific plate boundary zone, New Zealand. *J. Geophys. Res. Solid Earth.* 113(B3). <https://doi.org/10.1029/2006JB004594>
- Rowan, C. J., Roberts, A. P., Broadbent, T., 2009. Reductive diagenesis, magnetite dissolution, greigite growth and paleomagnetic smoothing in marine sediments: A new view. *Earth Planet. Sci. Lett.* 277(1-2), 223–235. <https://doi.org/10.1016/j.epsl.2008.10.016>
- Rudmin, M., Roberts, A.P., Horng, C.S., Mazurov, A., Savinova, O., Ruban, A., Kashapov, R., Veklich, M., 2018. Ferrimagnetic iron sulfide formation and methane venting across the Paleocene-Eocene Thermal Maximum in shallow marine sediments, ancient West Siberian Sea. *Geochem., Geophys., Geosys.* 19(1), pp.21-42. <https://doi.org/10.1002/2017GC007208>
- Sangode, S. J., Sinha, R., Phartiyal, B., Chauhan, O. S., Mazari, R. K., Bagati, T. N., et al., 2007. Environmental magnetic studies on some quaternary sediments of varied depositional settings in the Indian sub-continent. *Quat. Int.* 159, 102–118. <https://doi.org/10.1016/j.quaint.2006.08.015>
- Sangode, S. J., Suresh, N., Bagati, T. N., 2001. Godavari source in the Bengal fan sediments: Results from magnetic susceptibility dispersal pattern. *Curr. Sci.* 660–664. <https://www.jstor.org/stable/24104167>
- Shankar, U., Riedel, M., 2010. Seismic and heat flow constraints from the gas hydrate system in the Krishna–Godavari Basin, India. *Mar. Geol.* 276(1-4), 1-13. <https://doi.org/10.1016/j.margeo.2010.06.006>
- Shankar, U., Sain, K., Riedel, M., 2014. Assessment of gas hydrate stability zone and geothermal modeling of BSR in the Andaman Sea. *J. Asian Earth Sci.* 79, 358-365. <https://doi.org/10.1016/j.jseaes.2013.10.021>
- Shanmugam, G., Shrivastava, S. K., Das, B., 2009. Sandy debrites and tidalites of Pliocene reservoir sands in upperslope canyon environments, offshore Krishna–Godavari Basin (India): implications. *J. Sediment. Res.* 79(9), 736–756. <https://doi.org/10.2110/jsr.2009.076>
- Shi, M., Wu, H., Roberts, A. P., Zhang, S., Zhao, X., Li, H., et al., 2017. Tectonic, climatic, and diagenetic control of magnetic properties of sediments from Kumano Basin, Nankai margin, southwestern Japan. *Mar. Geol.* 391, 1–12. <https://doi.org/10.1016/j.margeo.2017.07.006>
- Snowball, I., Thompson, R., 1990. A stable chemical remanence in Holocene sediments. *J. Geophys. Res. Solid Earth.* 95(B4), 4471-4479. <https://doi.org/10.1029/JB095iB04p04471>
- Snowball, I. F., 1991. Magnetic hysteresis properties of greigite (Fe<sub>3</sub>S<sub>4</sub>) and a new occurrence in Holocene sediments from Swedish Lapland. *Phys. Earth Planet. Inter.* 68(1-2), 32-40. [https://doi.org/10.1016/0031-9201\(91\)90004-2](https://doi.org/10.1016/0031-9201(91)90004-2)

- Solomon, E. A., Spivack, A. J., Kastner, M., Torres, M. E., Robertson, G., 2014. Gas hydrate distribution and carbon sequestration through coupled microbial methanogenesis and silicate weathering in the Krishna–Godavari basin, offshore India. *Mar. Petrol. Geol.* 58, 233-253. <https://doi.org/10.1016/j.marpetgeo.2014.08.020>
- Sriram, G., Dewangan, P., Kumar, A., Mazumdar, A., Peketi, A., Mahale, V. P., 2020. Structural control on the methane seeps and shallow gas hydrate deposits in Krishna – Godavari Basin, Bay of Bengal in 36th International Geological Congress, November 9–14, 2020.
- Sriram, G., Dewangan, P., Ramprasad, T., Rama Rao, P., 2013. Anisotropic amplitude variation of the bottom-simulating reflector beneath fracture-filled gas hydrate deposit. *J. Geophys. Res. Solid Earth.* 118 (5), 2258–2274. <https://doi.org/10.1002/jgrb.50176>
- Suess, E., 2014. Marine cold seeps and their manifestations: geological control, biogeochemical criteria and environmental conditions. *Int. J. Earth Sci.* 103(7), 1889-1916. <https://doi.org/10.1007/s00531-014-1010-0>
- Tarduno, J. A., 1995. Superparamagnetism and reduction diagenesis in pelagic sediments: enhancement or depletion? *Geophys. Res. Lett.* 22(11), 1337-1340. <https://doi.org/10.1029/95GL00888>
- Teichert, B.M.A., Johnson, J.E., Solomon, E.A., Giosan, L., Rose, K., Kocherla, M., Connolly, E.C., Torres, M.E., 2014. Composition and origin of authigenic carbonates in the Krishna–Godavari and Mahanadi Basins, eastern continental margin of India. *Mar. Petrol. Geol.* 58, pp.438-460. <https://doi.org/10.1016/j.marpetgeo.2014.08.023>
- Torres, M.E., Hong, W.L., Solomon, E.A., Milliken, K., Kim, J.H., Sample, J.C., Teichert, B.M., Wallmann, K., 2020. Silicate weathering in anoxic marine sediment as a requirement for authigenic carbonate burial. *Earth Sci. Rev.* 200, 102960. <https://doi.org/10.1016/j.earscirev.2019.102960>
- Verwey, E. J. W., 1939. Electronic conduction of magnetite (Fe<sub>3</sub>O<sub>4</sub>) and its transition point at low temperatures. *Nature* 144(3642), 327. <https://doi.org/10.1038/144327b0>
- Verwey, E. J. W., 1947. Theory of the stability of lyophobic colloids. *J. Phys. Chem.* 51(3), 631-636. <https://doi.org/10.1021/j150453a001>
- Vigderovich, H., Liang, L., Herut, B., Wang, F., Wurgaft, E., Rubin-Blum, M., Sivan, O., 2019. Evidence for microbial iron reduction in the methanic sediments of the oligotrophic southeastern Mediterranean continental shelf. *Biogeosciences* 16(16), 3165-3181. <https://doi.org/10.5194/bg-16-3165-2019>
- Wallmann, K., Aloisi, G., Haeckel, M., Tishchenko, P., Pavlova, G., Greinert, J., Kutterolf, S. and Eisenhauer, A., 2008. Silicate weathering in anoxic marine sediments. *Geochimica et Cosmochimica Acta*, 72(12), pp.2895-2918. <https://doi.org/10.1016/j.gca.2008.03.026>
- Wellsbury, P., Goodman, K., Cragg, B. A., Parkes, R. J., 2000. The geomicrobiology of deep marine sediments from Blake Ridge containing methane hydrate (Sites 994, 995 and 997). In *Proceedings of the Ocean drilling program, Scientific results*, (Vol. 164, pp. 379–391). College Station, TX: Ocean Drilling Program.
- Xie, R., Wu, D., Liu, J., Sun, T., Liu, L., Wu, N. 2019. Geochemical Evidence of Metal-Driven Anaerobic Oxidation of Methane in the Shenhu Area, the South China Sea. *Int. J. Env. Res. Pub. He.* 16(19), 3559. <https://doi.org/10.3390/ijerph16193559>